Received: 1 July 2021 | Revised: 23 August 2021 | Accepted: 13 September 2021

DOI: 10.1002/dvdy.422

RESEARCH ARTICLE

Developmental Dynamics WILEY

Pax2a, but not *pax2b*, influences cell survival and periocular mesenchyme localization to facilitate zebrafish optic fissure closure

Sarah Lusk | **Kristen M. Kwan**

Department of Human Genetics, University of Utah, Salt Lake City, Utah, USA

Correspondence
Kristen M. Kwan, Department of Human Genetics, EIHG 5100, University of Utah, 15 North 2030 East, Salt Lake City, UT 84112, USA.
Email: kmkwan@genetics.utah.edu

Funding information
Eunice Kennedy Shriver National Institute of Child Health and Human Development, Grant/Award Number: T32 HD007491; National Eye Institute, Grant/Award Numbers: F31 EY030758, R01 EY025378

Abstract

Background: *Pax2* is required for optic fissure development in many organisms, including humans and zebrafish. Zebrafish loss-of-function mutations in *pax2a* display coloboma, yet the etiology of the morphogenetic defects is unclear. Further, *pax2* is duplicated in zebrafish, and a role for *pax2b* in optic fissure development has not been examined.

Results: Using a combination of imaging and molecular genetics, we interrogated a potential role for *pax2b* and examined how loss of *pax2* affects optic fissure development. Although optic fissure formation appears normal in *pax2* mutants, an endothelial-specific subset of periocular mesenchyme (POM) fails to initially localize within the optic fissure, yet both neural crest and endothelial-derived POM ectopically accumulate at later stages in *pax2a* and *pax2a; pax2b* mutants. Apoptosis is not up-regulated within the optic fissure in *pax2* mutants, yet cell death is increased in tissues outside of the optic fissure, and when apoptosis is inhibited, coloboma is partially rescued. In contrast to *pax2a*, loss of *pax2b* does not appear to affect optic fissure morphogenesis.

Conclusions: Our results suggest that *pax2a*, but not *pax2b*, supports cell survival outside of the optic fissure and POM abundance within it to facilitate optic fissure closure.

KEYWORDS

coloboma, optic cup, optic fissure, *pax2a*, *pax2b*, zebrafish

1 | INTRODUCTION

Vertebrate eye development begins as the eye anlage evaginates as an outpocketing of neural epithelium from the developing brain. These optic vesicle structures undergo precise morphogenetic events, including invagination, to form the bilayered optic cup, consisting of neural retina and retinal pigment epithelium. During this process, the connection between the optic vesicle and developing brain is constricted, forming the optic stalk, which initially serves to tether the eye and brain.[1-8] Concurrent with invagination is the formation of the optic fissure: two margins of neural retina and RPE form at the ventral surface of the optic cup and extend through the

stalk, creating a narrow cleft. This seam-like structure subsequently fuses along its proximodistal length to create an essential conduit used by vasculature cells to enter the eye, and retinal ganglion cell axons to exit the eye and connect with the brain. Defects in the development of the optic fissure can result in uveal coloboma, a congenital eye disorder that accounts for approximately 5% to 10% of pediatric blindness cases.[9-13]

Optic fissure development involves a number of key morphogenetic events. First, the optic fissure forms during optic cup morphogenesis, as seen by the emergence of two tissue margins at the ventral side of the eye. This is followed by optic fissure closure, during which the optic fissure margins align and come into close proximity, as described in chick and mouse.[14,15] The margins of the optic fissure abut each other at their basal surfaces, and the basal lamina that lines the fissure margins must break down in order for tissue fusion to begin.[16-19] Once the basement membrane is removed from the optic fissure margins, tissue fusion can proceed: the two tissue margins come together to create a continuous neural retina with RPE completely surrounding the eye and a seamless optic stalk. Cells that were once separated into two margins are realigned along a single continuous apical surface and interact with each other via stable adherens junctions.[14,15,19,20]

In addition to the epithelial optic cup and optic stalk tissues, a migratory cell population, the periocular mesenchyme (POM), is required for optic cup and fissure morphogenesis: defects in the POM are associated with coloboma.[21-24] Electron microscopy studies revealed that cells resembling the POM are in close contact with optic fissure cells,[18,25] and recent findings have suggested a potential role for these cells as a source of matrix metalloproteinase enzymes.[26] Further, removal of the developing eye away from sources of POM was associated with coloboma.[20] During optic cup morphogenesis, a component of the POM, the cranial neural crest, migrates around the optic cup and into the optic fissure.[19,20,27-30] Additionally, POM-derived endothelial cells come in contact with the optic fissure and are retained as the hyaloid vasculature is generated. It has been shown that during optic fissure closure, these endothelial cells localize to regions within the fissure where Laminin is absent, an indication of basement membrane breakdown.[19]

The genetic network underlying early eye development has been widely studied and includes a key set of conserved transcription factors. While our understanding of the genetic network underlying optic fissure development is somewhat less well studied, one well-known genetic regulator is the paired domain containing transcription factor, *pax2*. In vertebrates, *pax2* is expressed early in the optic vesicle and later in the ventral optic cup, optic fissure, and stalk, in addition to other organ systems including the developing ear, kidney, and brain.[31-39] As such, mutations in *pax2* lead to a variety of organ impairments, including defective optic nerve pathfinding, inner ear patterning, midbrain and hindbrain structure, and pronephric primordia patterning.[36,40-44] Humans heterozygous for loss-of-function or haploinsufficient mutations in *PAX2* present with renal coloboma syndrome, characterized as having both eye and kidney defects, including coloboma.[45-48] Additionally, both mice and zebrafish containing homozygous loss-of-function or haploinsufficient mutations in *pax2* display coloboma.[36,41,44,49]

While the zebrafish *pax2a* mutant has been studied for a significant time, there remain open questions regarding the morphogenetic defects leading to coloboma.[36] Recent work has begun to uncover defects in the timing of basement membrane degradation[26]; however, it remains unclear if formation of the optic fissure or stalk is affected at an earlier stage. Similarly, vascularization defects have now been described,[26] yet a quantitative analysis of neural crest-derived POM has not been undertaken. Previous studies have implicated cell death as an underlying cellular mechanism in coloboma of *pax2a* zebrafish mutants, but it is unclear if cell death is occurring specifically in the optic fissure during its development and morphogenesis.[50,51]

In addition to the outstanding questions surrounding the cellular mechanism underlying defective optic fissure morphogenesis in the zebrafish *pax2a* mutant, a potentially complicating factor in zebrafish is the duplication of the *pax2* gene. *Pax2b* has not been studied, yet both *pax2a* and *pax2b* are expressed in a spatially and temporally overlapping manner, including expression within the optic vesicle and ventral optic cup.[52] It is unknown whether *pax2b* contributes to zebrafish optic fissure development, and whether functional redundancy between the two *pax2* genes may mask other phenotypes when studying a single mutant.

In this study, we sought to characterize the cellular basis of coloboma in the zebrafish *pax2* mutant and interrogate a role for *pax2b*, using mutant alleles of *pax2a* and *pax2b*. Despite overlapping expression patterns and a high degree of protein identity, somewhat surprisingly, we did not uncover a novel role for *pax2b* in optic fissure formation or closure. Our analyses of *pax2a* and *pax2a; pax2b* mutants indicate that optic fissure formation occurs normally, however, as early as 24 hpf, the endothelial cells that contribute to the hyaloid vasculature fail to populate the optic fissure properly. We did not observe increased apoptosis specifically in the optic fissure; however, cell death is increased in other regions of the head (including midbrain-hindbrain boundary and POM) in

pax2a and *pax2a; pax2b* mutant embryos, and inhibition of apoptosis partially rescues the *pax2a* coloboma phenotype. Together, this study provides new insight into the role of *pax2a* and *pax2b* during zebrafish optic fissure development.

2 | RESULTS

2.1 | Loss-of-function mutations in *pax2a* but not *pax2b* result in coloboma in zebrafish embryos

Inactivating mutations in *pax2* result in coloboma in both humans and model organisms.[36,41,44,46-49] Zebrafish have two *pax2* genes, *pax2a* and *pax2b*, and while coloboma has been documented in zebrafish *pax2a* mutants, it remains unknown whether *pax2b* is involved in eye, and specifically, optic fissure development. Both proteins share similar domains, are highly conserved at the amino acid level (93% identical), and their gene expression patterns are overlapping, with specific expression in the optic stalk.[52] Humans contain only one copy of PAX2, thus we wanted to determine if a more severe phenotype in the zebrafish *pax2a* mutant might be masked by the presence of *pax2b*. To begin to address this, mutant alleles for both genes were acquired. The zebrafish $pax2a^{tu29a}$ allele has been described previously and is a well-characterized loss-of-function mutant that develops coloboma.[36,40] The $pax2b^{sa10953}$ mutant is an uncharacterized allele from the Zebrafish Mutation Project at the Wellcome Sanger Institute containing a splice site variant (G > A) in the first third of the transcript (schematized in Figure 1A).[53] To validate this allele and its consequence on the transcript, reverse transcription PCR was performed on wild-type and *pax2b* mutant cDNA using a combination of primers spanning the upstream and downstream exon and the intervening intron (exon 3, intron 3/4, and exon 5). In wild-type cDNA, primers in exon 3 and exon 5 amplified a band around the expected amplicon of 279 base pairs (Figure 1A,B, *primer set A*). Sanger sequencing of this band confirms that proper splicing takes place between exon 3 and exon 4 in wild-type embryos (Figure 1C). Using cDNA from *pax2b* mutants, no band is amplified with this primer set, suggestive of the large amplicon (21.7 kb) that would be generated due to disrupted splicing at the junction between exon 3 and intron 3/4 (Figure 1B). To confirm this and determine whether this splice disruption leads to nonsense-mediated decay, a reverse primer within the intron was used to amplify a band in the *pax2b* mutants (Figure 1A, *primer set B*). This set of primers effectively amplifies an RNA product (also detected to a lesser extent in the wild-type cDNA; Figure 1B), and the sequence of this product captures the exon/intron junction and the G > A point mutation of the $pax2b^{sa10953}$ allele (Figure 1C). The retention of intron 3/4 in *pax2b* mutants is predicted to lead to a premature stop codon and a truncated protein (Figure 1D). These results indicate that the *pax2b* mutation results in a defective transcript that does not seem to be degraded, but rather, is predicted to produce a protein truncated by two-thirds and lacking several domains important for protein function (schematized in Figure 1D).

To determine if *pax2b* plays a role in optic fissure development and if a more severe coloboma phenotype is masked due to genetic redundancy between *pax2a* and *pax2b*, heterozygous adults for $pax2a^{tu29a}$ (referred to as *pax2a* from here on) and $pax2b^{sa10953}$ (referred to as *pax2b*) were crossed to create a double heterozygous line, such that an incross yields single mutant embryos as well as $pax2a^{-/-}$; $pax2b^{-/-}$ double mutant embryos. These embryos were scored for coloboma at 55 hpf, a stage at which the optic fissure is mostly closed in wild-type embryos (Figure 2A-D; wt $11.35 \pm 5.61\%$ embryos with open fissure). In *pax2a* mutants, coloboma is apparent, with nearly complete penetrance (Figure 2B, *arrowhead*; 2M; *pax2a* $93.48 \pm 0.84\%$ embryos). In *pax2b* mutants, the eyes are properly pigmented and coloboma is not observed (Figure 2C, M; *pax2b* $4.34 \pm 2.70\%$ embryos). In *pax2a; pax2b* compound mutants, the coloboma phenotype is fully penetrant and appears indistinguishable from *pax2a* single mutants (Figure 2D, *arrowhead*; 2M; *pax2a; 2b* $100 \pm 0\%$ embryos). These results suggest that upon initial examination, *pax2b* is not functionally important for optic fissure development in zebrafish; however, both compound and single mutants were further analyzed to determine whether more subtle phenotypes or genetic interactions might be uncovered.

2.2 | Optic cup morphogenesis is not disrupted in *pax2* mutant embryos

The zebrafish *pax2a* mutant coloboma phenotype has been reported by several groups and has been described as a defect in optic fissure closure.[26,36,50,54] Despite this, assessments of optic cup morphogenesis, earlier in the developmental process, have not been reported; therefore, it is possible that initial formation of the optic fissure and stalk might be affected. To assay optic fissure and stalk formation, we imaged the optic cup at 24 hpf, when optic cup morphogenesis is complete. In all genotypes, the optic cup appears to form normally (Figure 2E-H). Lateral views of three-dimensional (3D) renderings reveal optic fissure and stalk morphology (Figure 2I-L):

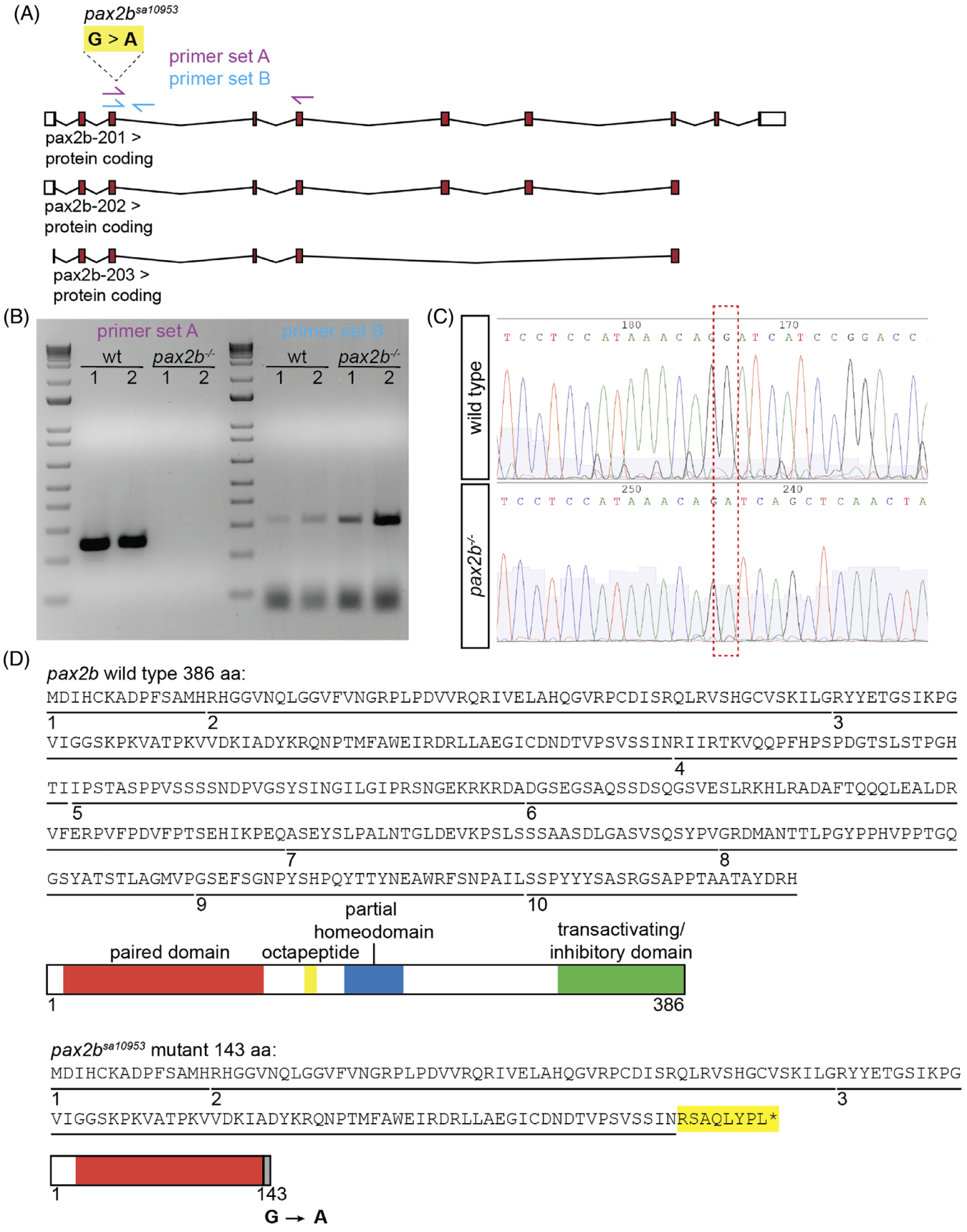

FIGURE 1 Legend on next page.

at the ventral side of the wild-type eye, the optic fissure is visible as a narrow cleft with closely apposed tissue margins. We quantified optic fissure formation by measuring the optic fissure opening angle (schematized in Figure 2N). We find no significant difference between wild-type and mutant optic fissure opening angles at 24 hpf (Figure 2N; wt 21.63 ± 1.28°, *pax2a* 17.55 ± 2.22°, *pax2b* 22.35 ± 3.21°, *pax2a;2b* 17.13 ± 4.38°). To assay optic stalk development, the volume of the optic stalk was measured using our 3D data sets: the optic stalk volume in *pax2* mutants is not significantly different compared to wild-type siblings (Figure 2O; wt $1.33 \pm 0.06 \times 10^5$ μm^3, *pax2a* $1.41 \pm 0.16 \times 10^5$ μm^3, *pax2b* $1.40 \pm 0.10 \times 10^5$ μm^3, *pax2a;2b* $1.23 \pm 0.10 \times 10^5$ μm^3). Taken together, these data indicate that even when *pax2a* and *pax2b* are mutated, the initial steps of optic fissure and stalk formation proceed normally, suggesting that morphogenetic defects contributing to coloboma arise after 24 hpf.

2.3 | The basement membrane does not properly break down in *pax2a* and *pax2a; pax2b* mutants

Following optic fissure formation, the optic fissure closes, during which the tissue margins surrounding the fissure undergo fusion. Work from many labs has helped to define distinct events during fusion.[14-20] Importantly, the basal lamina that lines each margin of the fissure must break down for tissue fusion to proceed. To begin to determine specific events in optic fissure development disrupted in *pax2* mutants, we first analyzed optic fissure basement membrane breakdown at different stages. The basement membrane is visualized using immunostaining for Laminin, a core extracellular matrix component. At 24 hpf, Laminin is visualized as a continuous basal surface lining each margin of the fissure in wild-type and mutant embryos (Figure 3A-D′). To quantify these image data, the depth of the fissure through the optic cup was determined, and the midpoint in the depth was selected as the "middle" section. At that single middle section, fluorescence intensity measurements were acquired and normalized within a rectangular region of interest around the optic fissure opening (schematized in Figure 3M; see Methods for more details). At 24 hpf, normalized Laminin fluorescence intensity is similar in wild-type embryos and *pax2a*, *pax2b*, and *pax2a; pax2b* mutants (Figure 3M; wt 0.31 ± 0.03, *pax2a* 0.31 ± 0.07, *pax2b* 0.31 ± 0.07, *pax2a;2b* 0.28 ± 0.08).

By 36 hpf, in wild-type embryos, Laminin fluorescence is discontinuous in the optic fissure, indicative of the initiation of basement membrane breakdown (Figure 3E-E′, *arrowhead*). In *pax2a* and *pax2a; pax2b* mutants, Laminin persists in the fissure and there are no regions where it is absent (Figure 3F-F′, H-H′, *asterisks*). In *pax2b* mutants, Laminin localization resembles that of wild-type siblings, suggesting that the breakdown of the optic fissure basement membrane is effectively initiated (Figure 3G-G′, *arrowhead*). Quantification of Laminin fluorescence intensity similarly reveals that *pax2a* and *pax2a; pax2b* mutants have more Laminin in the optic fissure compared to wild-type siblings, whereas there is no significant difference between *pax2b* mutants and wild-type siblings (Figure 3N; wt 0.18 ± 0.01, *pax2a* 0.26 ± 0.02, *pax2b* 0.20 ± 0.01, *pax2a;2b* 0.29 ± 0.05). These data suggest that at 36 hpf, breakdown of the Laminin basement membrane is appropriately initiated in *pax2b* mutants, but not *pax2a* or *pax2a; pax2b* double mutants.

At 48 hpf, Laminin is largely absent from the optic fissure in both wild-type and *pax2b* mutant embryos (Figure 3I-I′, K-K′, *arrowheads*). In *pax2a* and *pax2a; pax2b* mutant embryos, Laminin protein still completely

FIGURE 1 The *pax2b*^{sa10953} allele contains an essential splice site variant causing retention of intron 3/4 and a premature stop codon. (A) Using the zebrafish GRCz11 genome assembly, the *pax2b* gene is found on Chromosome 12: 45,799,982 to 45,876,387. Schematized are three predicted transcripts; the *pax2b*^{sa10953} allele contains a G > A mutation at site Chr 12:45872685 that is predicted to affect all transcripts. This schematic is shown reflected compared to the genomic organization for ease of interpretation, as *pax2b* lies on the reverse strand. Untranslated regions are depicted as white boxes, exons as red boxes, and introns as connecting lines. Two primer pairs are represented as arrows: primer set A (*magenta*) is located such that the forward primer is within exon 3 and the reverse primer is within exon 5; primer set B (*cyan*) has a forward primer in exon 3 and reverse primer in intron 3/4. (B) Image of an agarose gel containing RT-PCR products for each primer set using wild-type and *pax2b*^{sa10953} homozygous mutant cDNA. Using wild-type cDNA, primer set A amplifies a band with a predicted size of 279 base pairs. There is no amplification detected using *pax2b*^{sa10953} mutant cDNA, but the predicted size of this band is 21,718 base pairs. Using primer set B (predicted size of 346 base pairs), there is a faint band with wild-type cDNA and a stronger band with *pax2b*^{sa10953} mutant cDNA. (C) Sanger sequencing chromatograms for PCR products from wild-type and *pax2b*^{sa10953} homozygous mutant cDNA, cropped to show the mutation in *pax2b*^{sa10953} (*red box*). Downstream of the G > A site in the wild type is the sequence of exon 4, while the *pax2b* mutant contains the sequence of intron 3/4. (D) The predicted protein sequence for wild-type pax2b and the pax2b^{sa10953} allele. Each exon is underlined and numbered. Schematic displays the domains in the wild-type pax2b protein. In the *pax2b*^{sa10953} mutant, the disruption of the splice site junction leads to inclusion of amino acids from within intron 3/4 and an early stop codon (*yellow*, and *asterisk*). Schematic displays the predicted domains of the truncated pax2b^{sa10953} protein

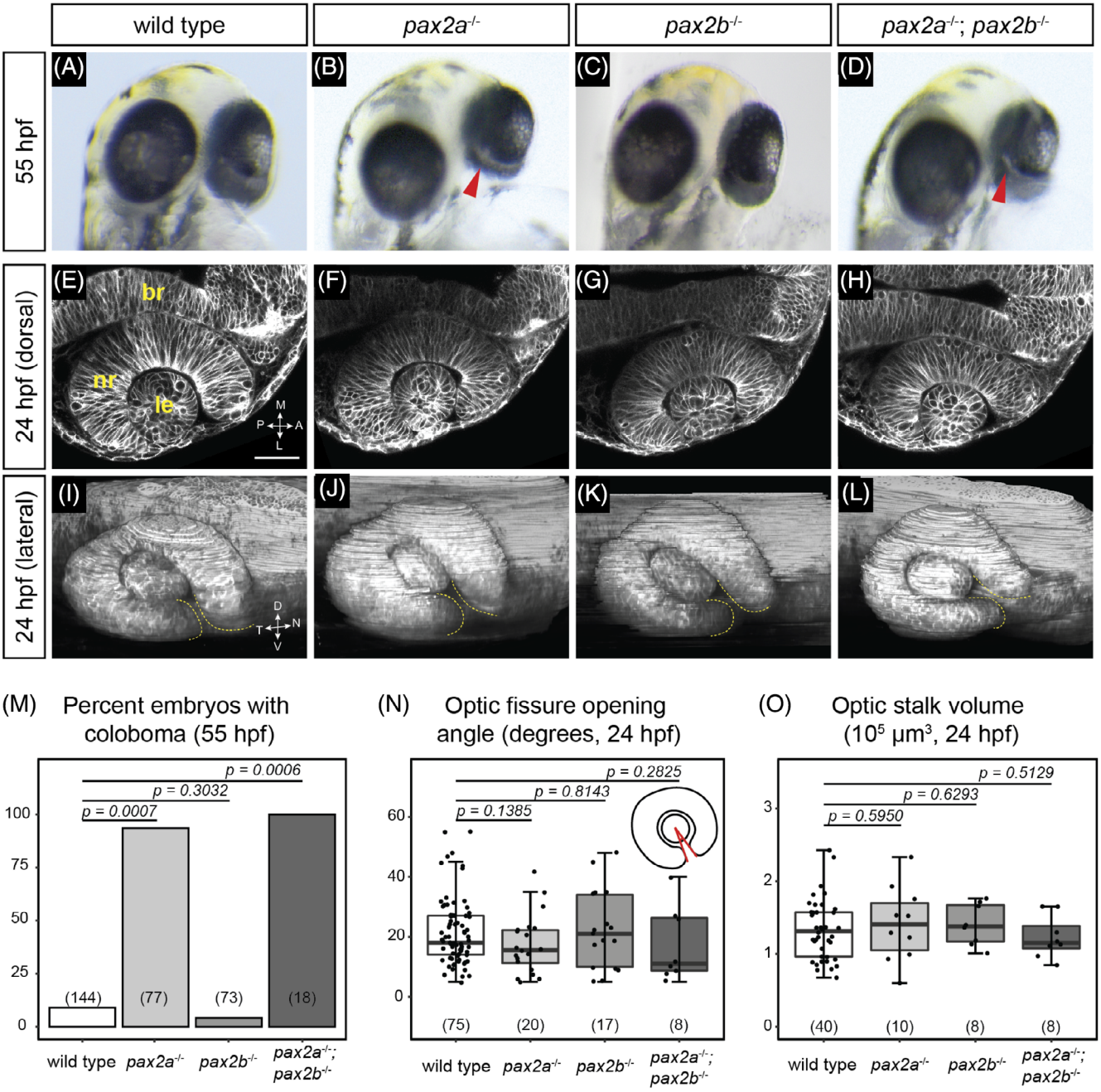

FIGURE 2 *pax2a* and *pax2a; pax2b* loss-of-function mutants display coloboma, but optic cup morphogenesis appears normal. (A-D) Eye phenotypes at 55 hpf. (A) Wild-type embryo. (B) *pax2a*^{tu29a} mutant embryo; coloboma is apparent as a region of hypopigmentation at the back of the eye (*red arrowhead*). (C) *pax2b*^{sa10953} mutant embryo; the eye is evenly pigmented, there is no apparent coloboma. (D) *pax2a*^{tu29a}; *pax2b*^{sa10953} mutant embryo; coloboma is apparent (*red arrowhead*). (E-L) Optic cup phenotypes at 24 hpf. (E) Wild-type, (F) *pax2a*^{tu29a} mutant, (G) *pax2b*^{sa10953} mutant, (H) and *pax2a*^{tu29a}; *pax2b*^{sa10953} mutant optic cup formation, single confocal slices. Dorsal view. Cell membranes, grayscale [*Tg(bactin2:EGFP-CAAX)*]. (I) Wild-type, (J) *pax2a*^{tu29a} mutant, (K) *pax2b*^{sa10953} mutant, (L) and *pax2a*^{tu29a}; *pax2b*^{sa10953} mutant optic cup formation, three-dimensional rendering. Lateral view. Cell membranes, grayscale [*Tg(bactin2:EGFP-CAAX)*]. Yellow dashed lines indicate optic fissure margins. (M) Penetrance of coloboma phenotype, 55 hpf. n (embryos) shown at base of graphs. (N) Quantification of optic fissure opening angle measurement, 24 hpf. n (embryos) shown at base of graphs. Schematic depicts the optic fissure opening angle measurement in which each ray (red) originates at the margins of the optic fissure and the vertex lies in the center of the lens. (O) Quantification of optic stalk volume, 24 hpf. n (embryos) shown at base of graphs. *P*-values for (M-O) were calculated using an unpaired Student's *t*-test. br, brain; le, lens; nr, neural retina. Scale bar: 50 µm

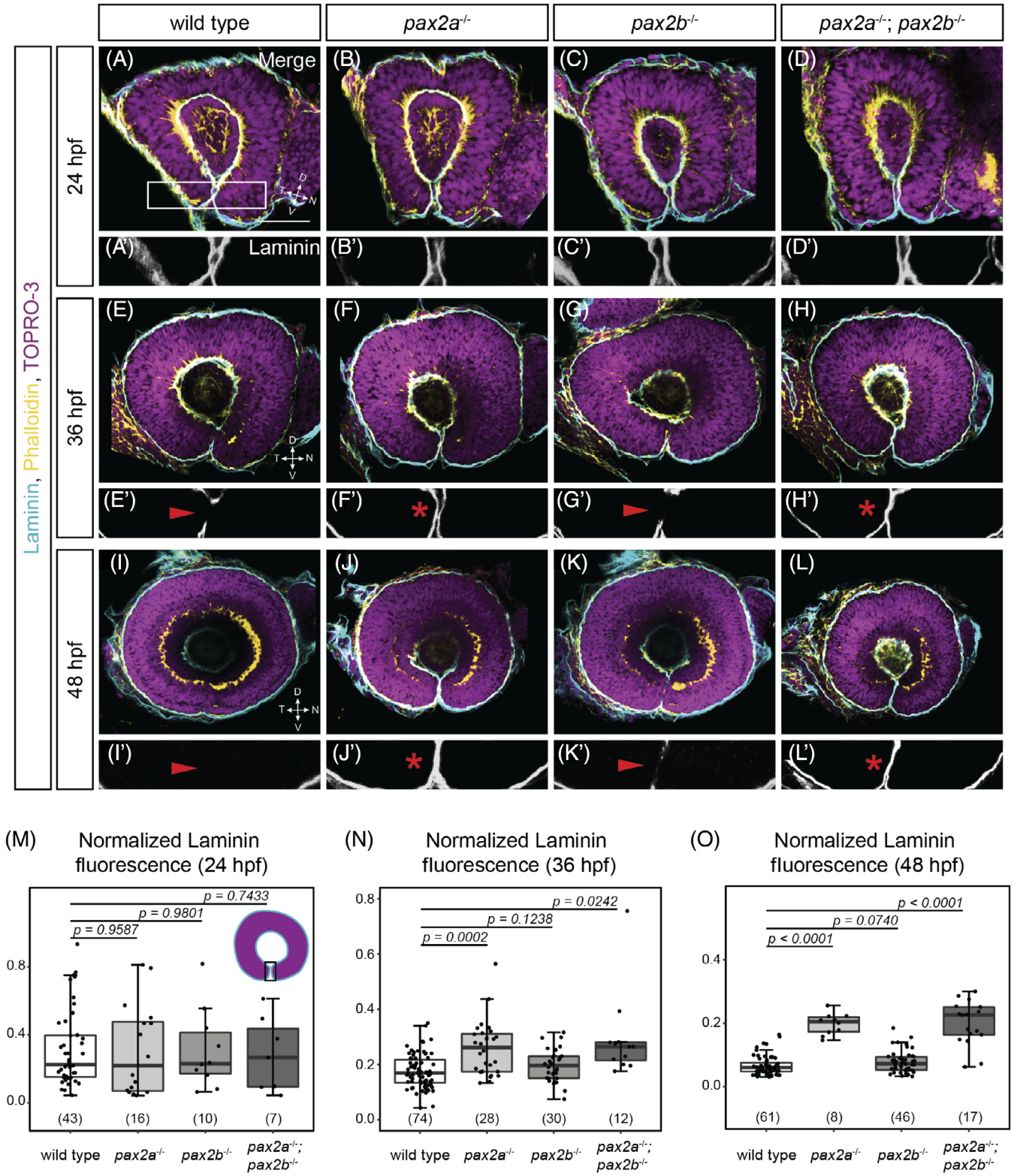

FIGURE 3 Legend on next page.

lines the fissure (Figure 3J-J', L-L', *asterisks*). When quantified, *pax2a* and *pax2a; pax2b* mutants have significantly greater normalized Laminin fluorescence intensity in the optic fissure compared to wild-type and *pax2b* mutant embryos (Figure 3O; wt 0.07 ± 0.00, *pax2a* 0.20 ± 0.01, *pax2b* 0.08 ± 0.01, *pax2a;2b* 0.20 ± 0.02). Taken together,

in *pax2a* mutants, but not *pax2b* mutants, the basement membrane fails to properly break down and is aberrantly retained within the optic fissure, a defect observed by 36 hpf.

2.4 | *Sox10*-positive neural crest cells properly localize to the optic fissure, but persist in *pax2a* and *pax2a; pax2b* mutants

To understand the basis of the failure of basement breakdown, we next examined the POM. The POM is a heterogeneous cell population comprised of both neural crest and mesoderm-derived mesenchymal cells, and it has been suggested to play a direct role in basement membrane breakdown during optic fissure closure.[19,20,26] These cells must migrate from a distance to arrive at the optic fissure. To determine whether the accumulation of these cells in the optic fissure is affected by loss of *pax2*, we used two different transgenes. To visualize neural crest cells, the *sox10:GFP* transgenic line was crossed to *pax2a*$^{+/-}$*; pax2b*$^{+/-}$ fish.[55] Embryos were injected with *mCherry-CAAX* mRNA, providing ubiquitous labeling to visualize eye and optic fissure morphology. These embryos were imaged live at several stages during optic fissure development.

By 24 hpf, neural crest cells have migrated to surround the optic cup and are observed within the optic fissure in wild-type, *pax2a*, *pax2b*, and *pax2a; pax2b* mutant embryos (Figure 4A-D; *arrowheads*). GFP-positive cells within the optic fissure were manually counted: the number of cells is not significantly different between wild-type and mutant genotypes (Figure 4M; wt 3.64 ± 0.29 cells, *pax2a* 3.92 ± 0.59 cells, *pax2b* 3.31 ± 0.29 cells, *pax2a;2b* 3.75 ± 0.25 cells). Similarly at 36 hpf, neural crest cells are observed within the optic fissure in wild-type and *pax2* mutant embryos (Figure 4E-H; *arrowheads*). Quantification of the GFP-positive cells in the optic fissure reveals no statistically significant difference between wild-type and *pax2* mutant genotypes (Figure 4N; wt 8.17 ± 0.69 cells, *pax2a* 8.57 ± 0.84 cells, *pax2b* 8.75 ± 0.90 cells, *pax2a;2b* 8.50 ± 0.91 cells). At 48 hpf, neural crest cells are still present within the optic fissure in wild-type, *pax2a*, *pax2b*, and *pax2a; pax2b* mutant embryos; however, in *pax2a* and *pax2a; pax2b* mutants, there are significantly more GFP-positive cells in the fissure than wild-type (Figure 4I-L, *arrowheads*; 4O; wt 4.37 ± 0.48 cells, *pax2a* 7.40 ± 1.19 cells, *pax2b* 5.50 ± 0.72 cells, *pax2a;2b* 6.50 ± 0.89 cells). Thus, while initial migration and localization of neural crest cells to the optic fissure appear to occur normally in *pax2a* and *pax2a; pax2b* mutants, as development proceeds, more *Tg(sox10:GFP)*-positive cells remain within the fissure than in wild-type embryos. This may be a consequence of the failure of optic fissure closure in *pax2a* and *pax2a; pax2b* mutants: while neural crest cells leave or are removed from the fissure as it closes in wild-type embryos, this process may be impaired in *pax2a* and *pax2a; pax2b* mutants.

2.5 | A subset of endothelial POM does not properly localize to the optic fissure by 24 hpf

Although labeling neural crest cells with the *sox10:GFP* transgene did not reveal significant defects in the initial accumulation of these cells within the optic fissure, we sought to visualize a specific subset of POM-derived endothelial cells that migrate through the optic fissure to generate the hyaloid vasculature. A second transgenic zebrafish line was used to label endothelial POM cells, *Tg(kdrl:mCherry-ras)*, and cell membranes were labeled ubiquitously using *Tg(bactin2:EGFP-CAAX)*.[56,57] These embryos were imaged live at several stages during optic fissure development.

FIGURE 3 The optic fissure basement membrane fails to break down in *pax2a* and *pax2a; pax2b* mutants. Whole-mount staining for Laminin (*cyan*), F-actin (*yellow*, phalloidin), and nuclei (*magenta*, TO-PRO-3) at 24 hpf (A-D), 36 hpf (E-H), and 48 hpf (I-L). Zoomed views of the optic fissure (A'-L', from boxed region (as shown in A) show Laminin alone (*grayscale*). All images are lateral views, single optical sections. (A) Wild-type, (B) *pax2a*^{tu29a}, (C) *pax2b*^{sa10953}, (D) and *pax2a*^{tu29a}*; pax2b*^{sa10953} embryos at 24 hpf. (A'-D′) Zoomed views of Laminin staining alone, showing Laminin staining in the optic fissure in all genotypes. (E) Wild-type, (F) *pax2a*^{tu29a}, (G) *pax2b*^{sa10953}, and (H) *pax2a*^{tu29a}*; pax2b*^{sa10953} embryos at 36 hpf. (E', G') Zoomed views of Laminin staining; staining is missing in wild-type and *pax2b*^{sa10953} mutant optic fissures (*red arrowheads*). (F′, H′) Zoomed views of Laminin staining, which persists and completely lines the optic fissure (*red asterisks*) in *pax2a*^{tu29a} and *pax2a*^{tu29a}*; pax2b*^{sa10953} mutants. (I) Wild-type, (J) *pax2a*^{tu29a}, (K) *pax2b*^{sa10953}, and (L) *pax2a*^{tu29a}*; pax2b*^{sa10953} embryos at 48 hpf. (I′, K′) Zoomed views of Laminin staining; staining is largely absent in wild-type and *pax2b*^{sa10953} mutant optic fissures (*red arrowheads*). (J', L') Zoomed views of Laminin staining, which continues to completely line the optic fissure in *pax2a*^{tu29a} and *pax2a*^{tu29a}*; pax2b*^{sa10953} mutants (*red asterisk*). (M-O) Quantification of Laminin fluorescence intensity normalized to TO-PRO-3 at a single mid-depth section using an ROI around the optic fissure, 24 hpf (M); 36 hpf (N); and 48 hpf (O). n (embryos) shown at base of graphs. *P*-values for (M-O) were calculated using an unpaired Student's *t*-test. Schematic (M) shows the region where the ROI was placed for quantification of the fluorescence intensity. Scale bar: 50 μm

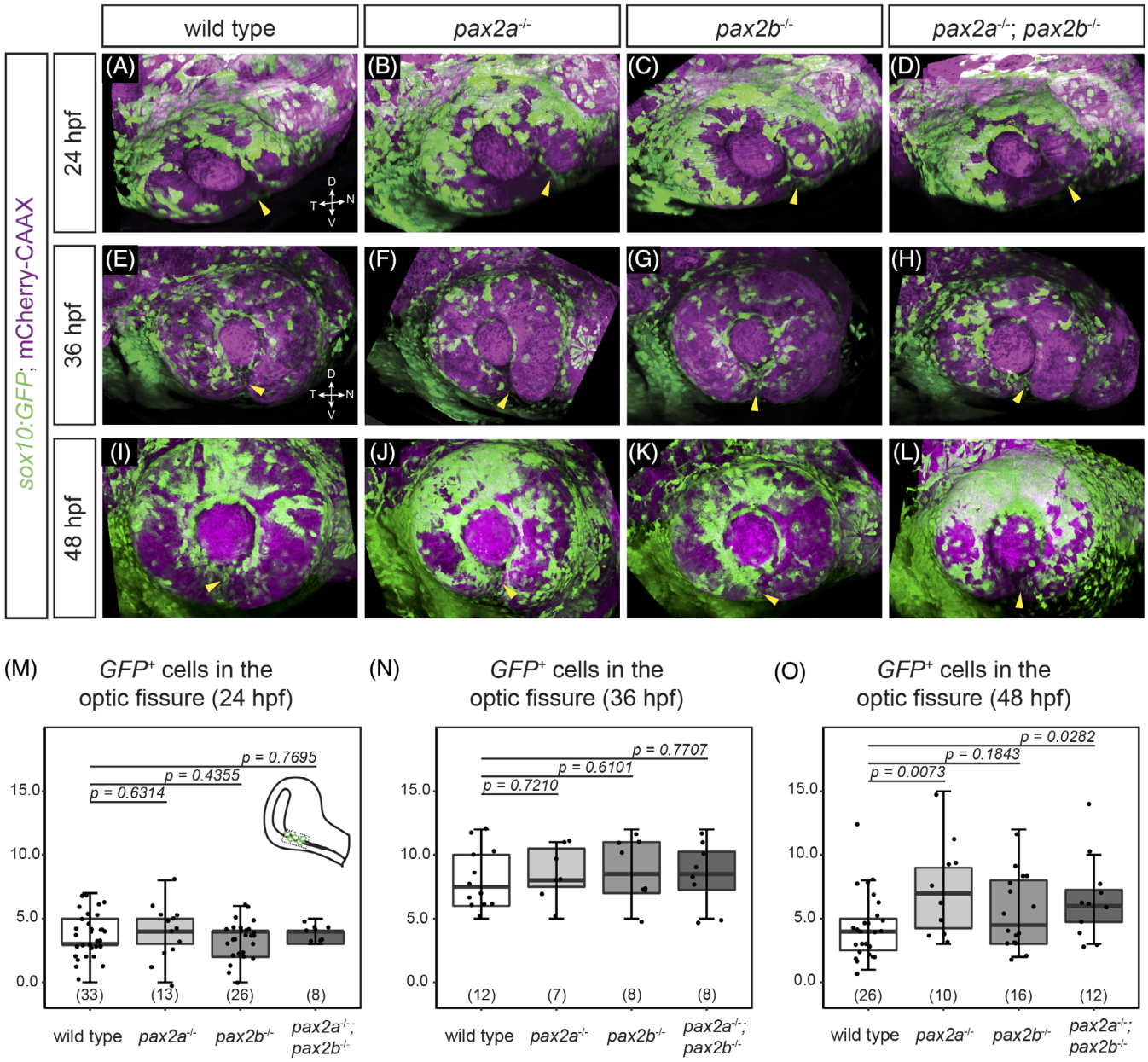

FIGURE 4 *Tg(sox10:GFP)*-positive neural crest cells properly localize in the optic fissure, but persist in *pax2a* and *pax2a; pax2b* mutants. Embryos visualized for neural crest (*green*; *Tg(sox10:GFP)*) and cell membranes (magenta; *mCherry-CAAX*) at 24 hpf (A-D), 36 hpf (E-H), and 48 hpf (I-L). All images are lateral views of three-dimensional renderings. (A) Wild-type, (B) $pax2a^{tu29a}$, (C) $pax2b^{sa10953}$, (D) and $pax2a^{tu29a}$; $pax2b^{sa10953}$ embryos at 24 hpf. GFP-positive cells are located within the fissure in each genotype (*yellow arrowheads*). (E) Wild-type, (F) $pax2a^{tu29a}$, (G) $pax2b^{sa10953}$, (H) and $pax2a^{tu29a}$; $pax2b^{sa10953}$ mutant embryos at 36 hpf. (I) Wild-type, (J) $pax2a^{tu29a}$, (K) $pax2b^{sa10953}$, (L) and $pax2a^{tu29a}$; $pax2b^{sa10953}$ mutant embryos at 48 hpf. (M-O) Quantification of GFP-positive cells throughout the depth of the optic fissure within the optic cup, 24 hpf (M); 36 hpf (N); and 48 hpf (O). n (embryos) shown at base of graphs. *P*-values for (M-O) were calculated using an unpaired Student's *t*-test. Schematic (M) shows the region of the optic fissure through the optic cup in which transgene-positive cells were quantified

By 24 hpf in wild-type embryos, *kdrl* transgene-labeled POM cells are found around the dorsal, anterior (nasal), and ventral circumference of the optic cup, in the optic fissure, and behind the lens (Figure 5A; *arrowhead*, optic fissure localization). In *pax2b* mutants, *kdrl* transgene-positive cells appear to correctly localize to the optic fissure and behind the lens (Figure 5C; *arrowhead*). In *pax2a* and *pax2a; pax2b* mutants, transgene-positive cells are observed around the dorsal optic cup; however, there are little or no cells present even near the optic fissure, and little or no cells within the fissure and behind the lens at this stage (Figure 5B, D; *asterisks*). To quantify

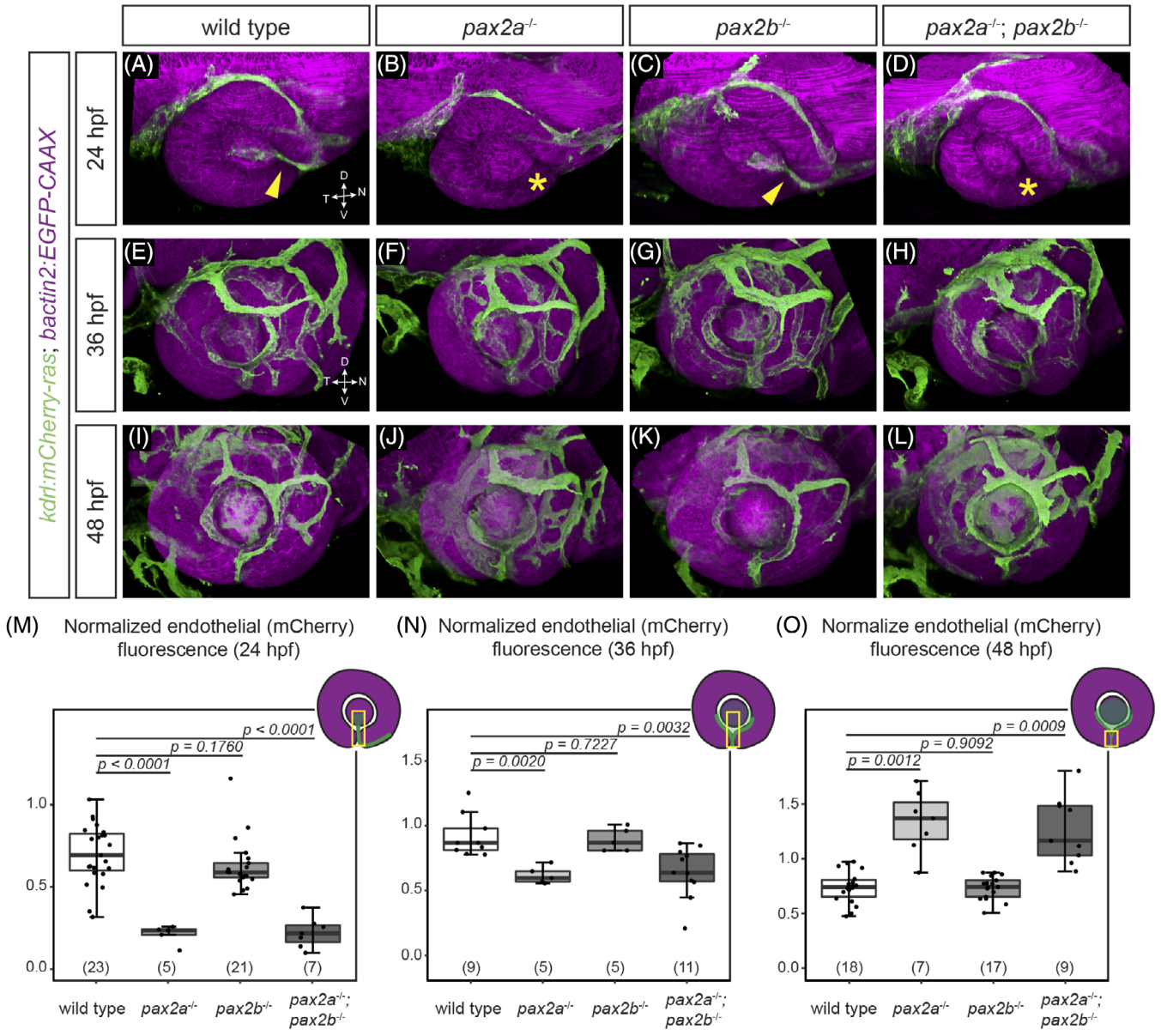

FIGURE 5 POM-derived endothelial cells do not properly populate the optic fissure in *pax2a* and *pax2a; pax2b* mutants. Embryos visualized for endothelial cells (*green*; *Tg(kdrl:mCherry-ras)*) and cell membranes (*magenta*; *Tg(bactin2:EGFP-CAAX)*) at 24 hpf (A-D), 36 hpf (E-H), and 48 hpf (I-L). All images are lateral views of three-dimensional renderings. (A) Wild-type, (B) *pax2a*^{tu29a}, (C) *pax2b*^{sa10953}, (D) and *pax2a*^{tu29a}*; pax2b*^{sa10953} embryos at 24 hpf. *kdrl* transgene-positive cells are located within the fissure (*yellow arrowhead*) and behind the lens in (A) wild-type and (C) *pax2b*^{sa10953}. *kdrl* transgene-positive cells are absent from this region (*yellow asterisk*) in (B) *pax2a*^{tu29a} and (D) *pax2a*^{tu29a}*; pax2b*^{sa10953} mutants. (E) Wild-type, (F) *pax2a*^{tu29a}, (G) *pax2b*^{sa10953}, (H) and *pax2a*^{tu29a}*; pax2b*^{sa10953} mutant embryos at 36 hpf. (I) Wild-type, (J) *pax2a*^{tu29a}, (K) *pax2b*^{sa10953}, (L) and *pax2a*^{tu29a}*; pax2b*^{sa10953} mutant embryos at 48 hpf. In contrast to 24 hpf, (J) *pax2a*^{tu29a} and (L) *pax2a*^{tu29a}*; pax2b*^{sa10953} mutants show increased POM-derived endothelial cells in the fissure region. (M-O) Quantification of endothelial cell (mCherry) fluorescence intensity normalized to GFP in a region of a maximum intensity projection of the optic fissure, 24 hpf (M); 36 hpf (N); and 48 hpf (O). n (embryos) shown at base of graphs. *P*-values for (M-O) were calculated using an unpaired Student's *t*-test. (M-O) Schematics show the specific region where the ROI was placed on the projected image for quantification of fluorescence intensity at 24 (M) and 36 hpf (N); the ROI did not include the lens region for quantification of fluorescence intensity at 48 hpf (O)

these observations, fluorescence intensity was measured and normalized in a rectangular region of interest encompassing the optic fissure and part of the lens, in a maximum intensity projection through the optic fissure (schematized in Figure 5M; see Methods for more details). At 24 hpf, there is significantly less *kdrl*-

transgene fluorescence in the optic fissure of *pax2a* and *pax2a; pax2b* mutants compared to wild-type sibling (Figure 5M; wt 0.56 ± 0.03, *pax2a* 0.17 ± 0.02, *pax2b* 0.50 ± 0.03, *pax2a;2b* 0.17 ± 0.03).

At 36 hpf, the superficial ocular vasculature network becomes more elaborated with dorsal branching, which appears grossly unaffected in *pax2* mutants (Figure 5E-H). Transgene-positive cells are observed within the fissure in wild-type embryos and all *pax2* mutant genotypes; however, quantification of transgene fluorescence intensity indicates that *pax2a* and *pax2a; pax2b* mutant embryos have significantly less fluorescence in the optic fissure and behind the lens than wild-type embryos (Figure 5N; wt 0.92 ± 0.05, *pax2a* 0.62 ± 0.03, *pax2b* 0.89 ± 0.04, *pax2a;2b* 0.64 ± 0.06). At 48 hpf, transgene-positive cells are found in the optic fissure of all genotypes; however, unlike earlier timepoints, fluorescence intensity is significantly increased in the optic fissure in *pax2a* and *pax2a; pax2b* mutant embryos compared to wild type (Figure 5I-L, O; wt 0.74 ± 0.03, *pax2a* 1.33 ± 0.11, *pax2b* 0.74 ± 0.03, *pax2a;2b* 1.27 ± 0.10).

These data indicate that as early as 24 hpf there is a defect in *pax2a* and *pax2a; pax2b* mutant embryos in which endothelial POM cells do not populate the optic fissure appropriately, yet by 48 hpf, there may be more endothelial cells (as assayed by fluorescence) compared to wild type. Additionally, for each stage assayed, *kdrl*-transgene fluorescence intensity in the optic fissure in *pax2b* mutants is indistinguishable from wild-type embryos, suggesting that POM accumulation in the optic fissure is unaffected by loss of pax2b.

2.6 | Apoptotic cell death is not observed in the optic fissure in wild-type or *pax2* mutant embryos

One potential mechanism proposed as underlying coloboma in the *pax2a* mutant is ectopic cell death.[50] Previous findings suggest increased cell death in *pax2a* mutants[40,50,51,54,58,59]; however, cell death has yet to be assayed specifically within the optic fissure margin cells during stages of formation and closure. Further, cell death in the *pax2b* mutant has not been previously examined. With this in mind, we sought to determine whether ectopic apoptotic cell death may be occurring in *pax2* mutants.

To assay optic fissure cell death, apoptotic cells were visualized using immunostaining for activated Caspase-3 at 24 hpf, 36 hpf, and 48 hpf (Figure 6A-L). To determine if cells within the optic fissure undergo apoptosis, activated Caspase-3-labeled cells specifically within the optic fissure were manually counted at each stage (schematized in Figure 6M). At no stage did we find a significant difference in the number of apoptotic optic fissure cells in wild-type or *pax2a*, *pax2b*, or *pax2a; pax2b* mutants (Figure 6M-O; 24hpf wt 0.27 ± 0.06 cells, *pax2a* 0.40 ± 0.15 cells, *pax2b* 0.27 ± 0.10 cells, *pax2a;2b* 0.21 ± 0.21 cells; 36hpf wt 0.28 ± 0.10 cells, *pax2a* 0.19 ± 0.11 cells, *pax2b* 0.09 ± 0.04 cells, *pax2a;2b* 0.18 ± 0.18 cells; 48hpf wt 0.68 ± 0.17 cells, *pax2a* 0.91 ± 0.24 cells, *pax2b* 0.56 ± 0.20 cells, *pax2a;2b* 0.92 ± 0.31 cells). While this method only captures apoptosis occurring at specific timepoints, we did not find evidence to suggest that ectopic apoptotic cell death specifically within the optic fissure might account for the *pax2a* mutant coloboma phenotype.

2.7 | Cell death is increased in the MHB and POM in *pax2a* and *pax2a; pax2b* mutants

Despite not observing significant activated Caspase-3-positive cells within the optic fissure in *pax2a* and *pax2a; pax2b* mutants, it has previously been shown that cells in the midbrain-hindbrain boundary (MHB) in *pax2a* mutants undergo programmed cell death.[40] One advantage of our whole-mount immunostaining for activated Caspase-3 is the opportunity to quantify cell death outside of the optic fissure in embryos of each genotype (Figure 6A-L; *arrowheads*). We found that at 24 hpf, apoptosis in the MHB is completely penetrant in *pax2a* and *pax2a; pax2b* mutant embryos, but it is not observed in wild-type or *pax2b* mutant embryos (Figure 6P). We also observed some embryos with cell death in the forebrain; however, when quantified, this did not correlate with any specific genotype (Figure 6P). Lastly, we quantified embryos for POM cell death. A greater percentage of *pax2a* and *pax2a; pax2b* mutant embryos exhibit apoptosis in the POM compared to wild-type or *pax2b* (Figure 6P). There are some caveats with this assay: the POM is a migratory population, and as such, the fraction of cells captured in each image can be variable, and fixed immunostaining provides only a snapshot of the cells at a given time. Overall, these data suggest that while apoptosis is not increased in the optic fissure of *pax2a* and *pax2a; pax2b* mutants, apoptosis is increased in the MHB and POM of these embryos.

2.8 | Apoptosis does contribute to the *pax2a* and *pax2a; pax2b* mutant coloboma phenotype

Although apoptotic cell death specifically in the optic fissure was essentially undetectable and is therefore unlikely to be the cause of coloboma in *pax2a* and *pax2a;*

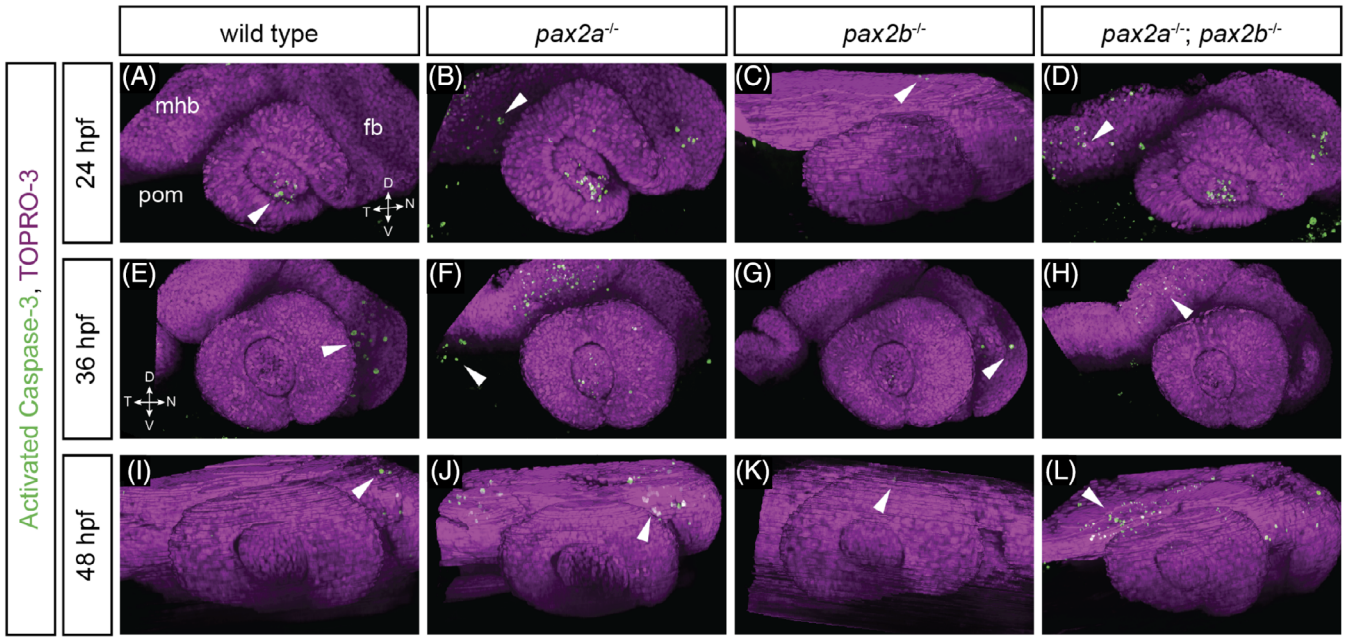

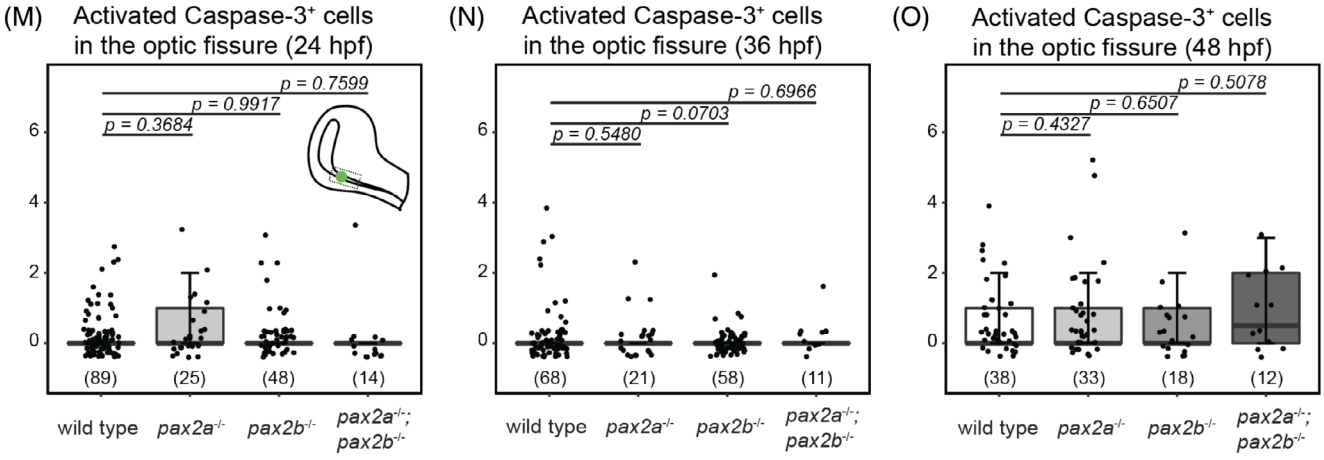

(P) Percent embryos with >5 Activated Caspase-3+ cells (24 hpf)

	forebrain	MHB	POM
wild type (n)	21.3% (19/89)	1.0% (1/70)	14.7% (13/89)
pax2a$^{-/-}$ (n)	21.0% (6/25)	100.0% (18/18)	39.7% (12/25)
pax2b$^{-/-}$ (n)	24.5% (8/48)	0.0% (0/40)	19.0% (8/48)
pax2a$^{-/-}$; *pax2b*$^{-/-}$ (n)	16.1% (2/14)	100.0% (10/10)	38.4% (6/14)

FIGURE 6 Minimal apoptotic cell death is observed in the optic fissure, but is increased in the MHB and POM in *pax2a* and *pax2a; pax2b* mutants. Whole-mount immunofluorescence for cell death (*green*; activated Caspase-3) and nuclei (*magenta*; TO-PRO-3) at 24 hpf (A-D), 36 hpf (E-H), and 48 hpf (I-L). All images are lateral views of three-dimensional renderings. (A) Wild-type, (B) *pax2a*^{tu29a}, (C) *pax2b*^{sa10953}, (D) and *pax2a*^{tu29a}; *pax2b*^{sa10953} embryos at 24 hpf. (E) Wild-type, (F) *pax2a*^{tu29a}, (G) *pax2b*^{sa10953}, (H) and *pax2a*^{tu29a}; *pax2b*^{sa10953} embryos at 36 hpf. (I) Wild-type, (J) *pax2a*^{tu29a}, (K) *pax2b*^{sa10953}, (L) and *pax2a*^{tu29a}; *pax2b*^{sa10953} embryos at 48 hpf. *White arrowheads*, examples of cells labeled with activated Caspase-3 elsewhere in the optic cup, brain, or POM. (M-O) Quantification of total number of activated Caspase-3-positive cells throughout the depth of the optic fissure within the optic cup, at 24 hpf (M); 36 hpf (N); and 48 hpf (O). n (embryos) shown at base of graphs. *P*-values for (M-O) were calculated using an unpaired Student's *t*-test. Schematic (M) shows the specific region of the optic fissure through the optic cup in which activated Caspase-3-positive cells were quantified.
(P) Table summarizing number of embryos at 24 hpf containing five or more activated Caspase-3-positive cells located in the forebrain, MHB, and POM for each genotype. mhb, *midbrain-hindbrain boundary*; pom, *periocular mesenchyme*; fb, *forebrain*

pax2b mutants, it remains unknown if apoptosis in other structures such as the MHB or POM could be a contributing factor. To test this hypothesis, we inhibited cell death by injecting mRNA encoding Bcl-xL, a Bcl-2 family member that acts as an anti-apoptotic factor by altering the mitochondrial membrane to prevent the release of mitochondrial contents including Cytochrome *C*.[60] To confirm that Bcl-xL effectively inhibits apoptotic cell death, embryos were injected with 100 pg of *Bcl-xL* mRNA at the one-cell stage, raised to 24 hpf, and fixed and immunostained for activated Caspase-3 (Figure 7A-D). Activated Caspase-3-labeled cells were manually counted in the optic fissure, forebrain, MHB, and POM (Figure 7E, F). We again observed no significant cell death occurring within the optic fissure in each genotype at 24 hpf (Figure 7E). Importantly, comparing Figures 6P and 7F, we observed fewer embryos with cell death occurring in the forebrain (wt 21.3% vs injected 11.8%; *pax2a* 21.0% vs injected 0.0%; *pax2b* 24.5% vs injected 6.7%; *pax2a;2b* 16.1% vs injected 11.1%), the MHB (wt 1.0% vs injected 0.0%; *pax2a* 100.0% vs injected 14.3%; *pax2b* 0.0% vs injected 0.0%; *pax2a;2b* 100.0% vs injected 0.0%), and POM (wt 14.7% vs injected 5.9%; *pax2a* 39.7% vs injected 0.0%; *pax2b* 19.0% vs injected 6.7%; *pax2a;2b* 38.4% vs injected 0.0%). Therefore, Bcl-xL mRNA injection is an effective tool to inhibit apoptosis.

Next, we wanted to determine if apoptotic cell death contributes the *pax2a* mutant coloboma phenotype. Embryos were injected with 100 pg of *Bcl-xL* mRNA and raised to 55 hpf when the optic fissure has generally closed in an uninjected wild-type embryo (Figure 7G-J). Uninjected control siblings and injected embryos were scored for coloboma. As previously shown (Figure 2A–D, M), uninjected *pax2a* and *pax2a; pax2b* mutants exhibit coloboma, while *pax2b* mutants do not (Figure 7K; wt uninjected $9.30 \pm 9.30\%$ embryos, *pax2a* uninjected $92.26 \pm 0.60\%$ embryos, *pax2b* uninjected $3.13 \pm 3.13\%$ embryos, *pax2a;2b* uninjected $100 \pm 0\%$ embryos). When *Bcl-xL* mRNA is injected and apoptosis is inhibited, the coloboma phenotype in *pax2a* and *pax2a; pax2b* mutants is partially rescued (Figure 7H, J, K; wt injected $5.95 \pm 1.95\%$ embryos, *pax2a* injected $43.42 \pm 6.58\%$ embryos, *pax2b* injected $3.80 \pm 1.76\%$ embryos, *pax2a;2b* injected $42.14 \pm 22.14\%$ embryos). This partial rescue suggests that cell death is one cellular mechanism that contributes in the *pax2a* and *pax2a; pax2b* mutant coloboma phenotype.

3 | DISCUSSION

We describe here several steps of optic fissure morphogenesis that are disrupted in *pax2a* and *pax2a; pax2b* mutants. In accordance with recent work, we find that the basal lamina lining the optic fissure margins fails to break down in *pax2a* and *pax2a; pax2b* mutants and is retained through optic fissure closure stages.[26] We show that the hyaloid vasculature is affected in these mutants; cells do not properly populate the mutant optic fissure as early as 24 hpf, despite greater endothelial fluorescence intensity within the optic fissure by 48 hpf. We do not observe a defect in neural crest-derived POM in the optic fissure until 48 hpf; however, this late phenotype may be an indirect effect of the fissure remaining open. It remains unknown whether in the *pax2a* mutant, the endothelial POM cells fail to correctly migrate to the optic fissure during development, or if they lack survival cues during this process. These questions can only be answered by looking more closely at this early stage of optic fissure development through timelapse imaging analysis.

We observe that neural crest-derived POM is largely unaffected in *pax2* mutants, yet initial endothelial cell recruitment to the optic fissure is impaired. It has previously been suggested that hyaloid vasculature cells may be involved in basement membrane breakdown during optic fissure closure, and our findings are consistent with this model.[19,20,26] Our results suggest that defects in POM localization are associated with failed optic fissure closure and coloboma. Despite the lack of endothelial cells in the optic fissure in *pax2* mutants at 24 hpf, they appear to be more abundant by 48 hpf, suggesting a crucial developmental time window for endothelial cells to take part in optic fissure closure. When this window has passed, the overabundance of cells is not sufficient to aid in optic fissure closure and coloboma still occurs, indicating that the early deficit may be the underlying issue. An interesting subject of future studies would be to determine whether POM cell activity or other aspects of fissure morphogenesis are further impaired or delayed in *pax2* mutants given accumulation and overabundance of these cells at 48 hpf. Further, the mechanism by which *pax2a* might promote POM survival and localization to the optic fissure at the correct time during optic fissure morphogenesis remains unclear. In the future, it will be interesting to understand how *pax2a* might also impact development and function of the hyaloid network.

A recent study examined optic fissure closure in the zebrafish *pax2a* mutant, including characterizing the basement membrane and vasculature within the fissure.[26] Similar to the results here, they reported that the basement membrane fails to be degraded in the mutant optic fissure. Endothelial cells were also analyzed, and although similar observations were made at particular overlapping timepoints, the prior work did not extend their quantitative analysis as early as ours. Strikingly, we find a defect in endothelial cell recruitment as early as

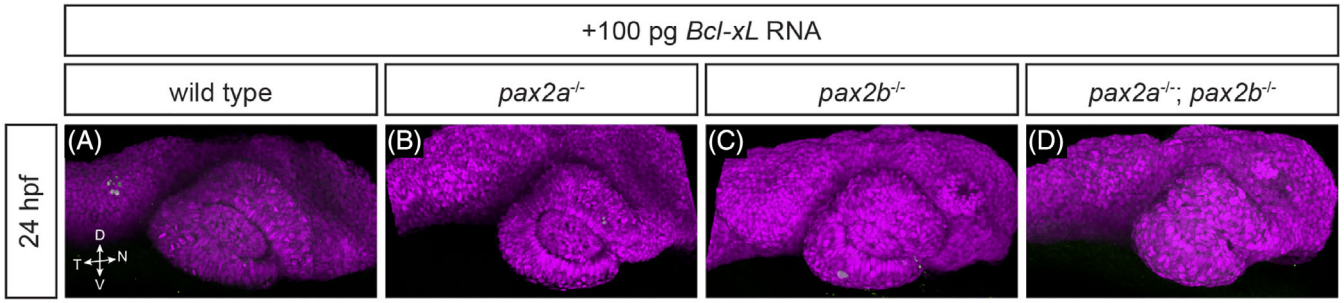

(E) Activated Caspase-3⁺ cells in the optic fissure + *Bcl-xL* RNA (24 hpf)

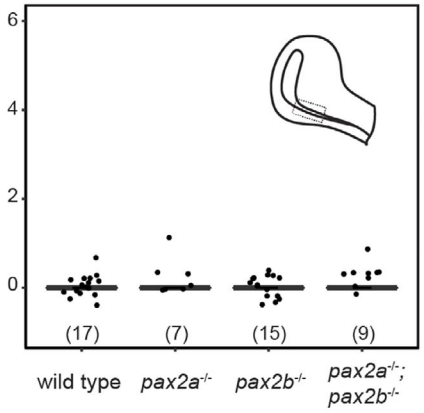

(F) Percent embryos + 100 pg *Bcl-xL* RNA with >5 Activated Caspase-3⁺ cells (24 hpf)

	forebrain	MHB	POM
wild type (n)	11.8% (2/17)	0.0% (0/16)	5.9% (1/17)
pax2a$^{-/-}$ (n)	0.0% (0/7)	14.3% (1/6)	0.0% (0/7)
pax2b$^{-/-}$ (n)	6.7% (1/15)	0.0% (0/13)	6.7% (1/15)
pax2a$^{-/-}$; *pax2b*$^{-/-}$ (n)	11.1% (0/9)	0.0% (0/9)	0.0% (0/9)

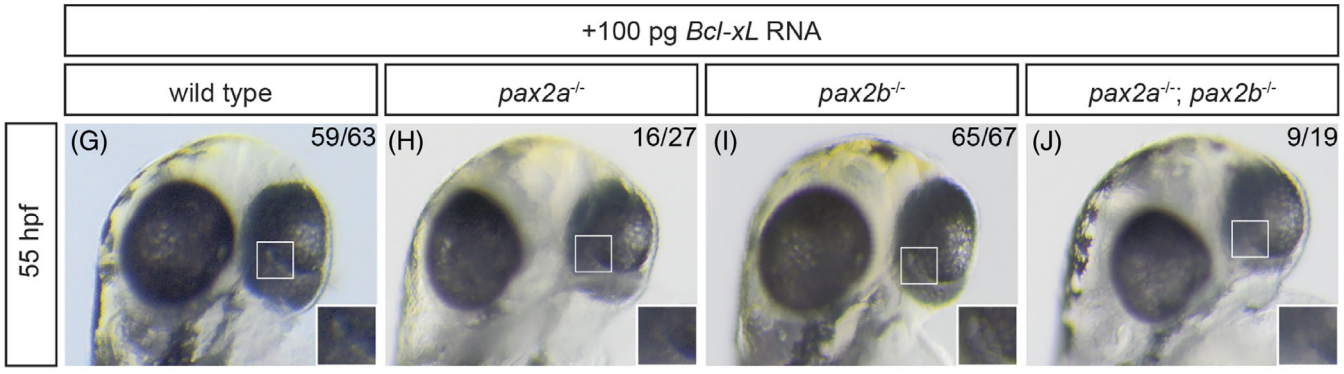

(K) Percent embryos with coloboma (55 hpf)

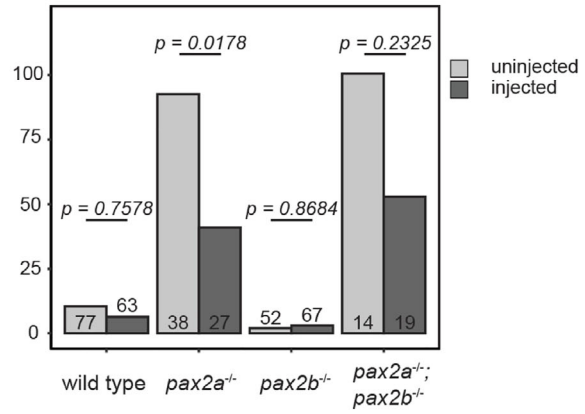

FIGURE 7 Legend on next page.

24 hpf, in which initial recruitment to the fissure is impaired, which may suggest an early role for *pax2a* in supporting the vasculature hours prior to when optic fissure closure is actually initiated. Future work could address specific roles for *pax2* during these early time windows.

For the first time, we directly quantify apoptotic cell death in the zebrafish *pax2a* mutant during optic fissure formation and closure. We do not detect fissure cells undergoing apoptosis, yet global inhibition of apoptotic cell death using Bcl-xL partially rescues the coloboma phenotype, suggesting that cell death is indeed involved in this defect. We observe increased proportions of apoptotic cells in *pax2a* mutants in the MHB where it is strongly expressed, but also in POM that do not express *pax2a*, suggesting a potential non-cell autonomous effect. While POM cells are known to be involved in optic fissure development (defects in POM genes result in coloboma),[20,22,23,28,61,62] a potential role for the MHB in this process has not been investigated. Future studies could utilize cell transplantation experiments to dissect specific contributions of different tissues to the process of optic fissure development.

A previous study found a role for *pax2a* in regulating necroptotic cell death via a *fadd*-dependent mechanism.[51] While this analysis examined RIP1/RIP3, a downstream kinase in the necroptosis pathway, it remains unclear which cells, fissure margin cells or POM within the optic fissure, are undergoing necroptotic cell death, and if other cells outside of the fissure (eg, MHB or POM) are also undergoing necroptosis. Our analysis of programmed cell death only examined cells undergoing apoptosis, thus taken together, an open question remains as to how *pax2* controls cell survival via different mechanisms and in multiple cell populations.

We show that apoptosis is one mechanism contributing to the *pax2a* mutant coloboma phenotype, and work by others has shown that necroptosis may also be responsible, but there are likely additional mechanisms at play. *Pax2a* is a transcription factor, and research has begun to uncover downstream transcriptional targets.[63] Uncovering the molecular identities of other factors in the optic fissure genetic network will further aid in understanding the molecular mechanism by which *pax2a* regulates optic fissure development.

Lastly, a potential role of *pax2b* in optic fissure morphogenesis remains unclear. *Pax2b* is strongly expressed in similar tissues as *pax2a*, including the optic vesicle, ventral optic cup, optic stalk, and optic fissure, thus it is surprising that our evidence suggests that the *pax2b* loss-of-function mutants lack an eye phenotype, and compound mutants do not have a more severe phenotype than the single *pax2a* mutant. It remains possible that *pax2b* mutants may have defects later during eye development, or in other organs where it is expressed, but this analysis lies outside of the scope of this study. Our data indicate that in the context of zebrafish *pax2*, the single *pax2a* mutant is the appropriate model for study of coloboma.

4 | EXPERIMENTAL PROCEDURES

4.1 | Zebrafish Husbandry and mutant/transgenic lines

All zebrafish (*Danio rerio*) husbandry was performed under standard conditions in accordance with University of Utah Institutional Animal Care and Use Committee (IACUC) Protocol approval (Protocol #21-01007). Embryos (Tu or TL strains) were raised at 28.5°C to 30°C and staged according to time post-fertilization and morphology.[64] Melanization was prevented with 0.003% 1-phenyl-2-thiourea (P7629, Sigma-Aldrich) after gastrulation when necessary. Mutant alleles are *pax2a*^{tu29a40} and *pax2b*^{sa10953}.[53] Transgenic alleles used are *Tg(sox10:GFP)*^{ba4},[55] *Tg(kdrl:ras-mCherry)*^{s896Tg},[56] and *Tg(bactin2:EGFP-CAAX)*^{z200}.[57]

FIGURE 7 Inhibition of apoptosis with *Bcl-xL* RNA rescues cell death within the MHB and POM and partially rescues coloboma in *pax2a* and *pax2a; pax2b* mutants. (A-D) Whole-mount immunofluorescence for cell death (*green*; activated Caspase-3) and nuclei (*magenta*; TO-PRO-3) at 24 hpf for (A) wild-type, (B) *pax2a*^{tu29a}, (C) *pax2b*^{sa10953}, (D) and *pax2a*^{tu29a}*; pax2b*^{sa10953} mutant embryos injected with 100 pg *Bcl-xL* RNA. Images are lateral views of three-dimensional renderings. (E) Quantification of total number of activated Caspase-3-positive cells throughout the depth of the optic fissure within the optic cup in *Bcl-xL*-injected embryos, 24 hpf. n (embryos) shown at base of graphs. Schematic (E) shows the region of the optic fissure through the optic cup in which activated Caspase-3-positive cells were quantified. (F) Table summarizing number of *Bcl-xL*-injected embryos at 24 hpf containing five or more activated Caspase-3-positive cells located in the forebrain, MHB, and POM for each genotype. (G-J) Phenotype of (G) wild-type, (H) *pax2a*^{tu29a}, (I) *pax2b*^{sa10953}, (J) and *pax2a*^{tu29a}*; pax2b*^{sa10953} mutant embryos injected with *Bcl-xL* RNA at 55 hpf. In each example, the eye is evenly pigmented and does not exhibit coloboma. Zoomed insets show the optic nerve head and medial optic fissure where closure has occurred in each genotype. The fraction in the bottom right corner represents the number of embryos without coloboma over the total number of embryos for each genotype. (K) Penetrance of coloboma phenotype in uninjected embryos (light gray bars) compared to embryos injected with 100 pg *Bcl-xL* RNA (dark gray bars), 55 hpf. n (embryos) shown at base of graphs. *P*-values were calculated using an unpaired Student's *t*-test

For genotyping, genomic DNA was extracted from single embryos or adult fins, incubated at 95°C in 0.05 M NaOH for 30 minutes, then neutralized with 1 M Tris pH 8.0. The *pax2a* locus was genotyped using a CAPS assay[65] with the following primers: NOI_F 5′-CATG CAGAAGCTAACCGTTG-3′; NOI_R 5′-GGCACTGAA AGAGCACAGG-3′. The *pax2a*^{tu29a} mutation eliminates a TaqI-v2 cut site, while the wild-type allele is cut. The *pax2b* locus was genotyped using a dCAPS assay[66] with the following primers: pax2b_F 5′-GCCTGGGAGATCCGGGACA GGCTGCTGGCGGAGGGCATCTGTGATAACGACACCG TCCCCAGTGTCTCCTCCATAAACCG-3′; pax2b_R 5′-G GCGCGTACACCTGGTAACC-3′. The dCAPS forward primer create a mismatch that generates an AgeI cut site in the wild-type allele, while the *pax2b*^{sa10953} mutant allele is uncut.

4.2 | RNA synthesis and nucleic acid injections

pCS2 templates (pCS2-EGFP-CAAX, pCS2-mCherry-CAAX, pCS2-Bcl-xL) were linearized with NotI-HF (R3189L, NEB) and capped RNA was synthesized using the mMessage mMachine SP6 kit (AM1340, Invitrogen). RNA was purified using the RNeasy Mini Kit (74104, Qiagen) and ethanol precipitated. For fluorescent proteins, 100-200 pg RNA was injected into one-cell embryos. To inhibit apoptosis, 100 pg Bcl-xL RNA was injected into one-cell embryos.

4.3 | Reverse transcription PCR

Embryos were pooled at 24 hpf (n = 30) and immediately homogenized using the QIAshredder column (79654, Qiagen). Total RNA was then extracted using the RNeasy Mini Kit (74104, Qiagen) and stored at −80°C until use. cDNA was synthesized using the iScript cDNA Synthesis kit (1708890, Bio-Rad) following the manufacturer's recommendations, such that 1 μg of RNA was loaded into each reaction. Three biological replicates were collected for each genotype. RT-PCR was performed using cDNA from wild-type samples and *pax2b* mutant samples with the following primers used: primer set A exon3_forward 5′-GCATCTGTGATAACGACACCG-3′, intron_reverse 5′-GGCGCGTACACCTGGTAACC-3′; primer set B exon5_reverse 5′-GCATCTCGTTTCCTCTTTTC-3′. PCR products were gel extracted and Sanger sequenced.

4.4 | Coloboma scoring

Embryos were individually screened and scored for coloboma at 52 to 55 hpf using an Olympus SZX16 stereomicroscope. The phenotype was scored by viewing the back of the eye and focusing at the depth of the RPE; embryos that were scored as positive for coloboma had eyes that displayed an expanded region lacking pigmentation in the area of the optic nerve head either unilaterally or bilaterally. This area was distinctly wider and more open than the rest of the optic fissure that was undergoing fusion at the ventral side of the optic cup. All genetic experiments were scored blindly. Embryos were subsequently genotyped as described above.

4.5 | Antibody staining

Embryos were raised until the stage of interest and fixed in 4% paraformaldehyde (15710, Electron Microscopy Science) overnight at 4°C or for 2 hours at room temperature. Embryos were permeabilized in PBST (PBS with 0.1% Triton X-100) and blocked in PBST with 2% bovine serum albumin for 1 hour at room temperature. Primary antibodies were diluted in blocking solution and incubated overnight at 4°C or for 4 hours at room temperature. Secondary antibodies were co-incubated with 1 μM TO-PRO-3 iodide (Life Technologies, T3605) overnight at 4°C. Primary antibodies were: anti-Laminin (L9393, Sigma-Aldrich; 1:200), Alexa Fluor conjugated-568 Phalloidin (A12380, Invitrogen; 1:500) and anti-activated Caspase-3 (#559565, BD Pharmingen;1:200). Secondary antibody was Alexa Fluor 488-conjugated goat anti-rabbit (Life Technologies, A-1108; 1:200). Embryos were cleared in 70% glycerol for imaging.

4.6 | Imaging

For confocal imaging, both live and fixed, embryos were embedded in 1.6% low melting point agarose in E3 or PBS in PELCO glass bottom dishes (14 027, Ted Pella). Images were acquired using either a Zeiss LSM710 or LSM880 laser-scanning confocal microscope. All imaging was performed with a 40x water immersion objective (1.2 NA). Data sets were acquired with the following parameters: 512 × 512; voxel size 0.69 × 0.69 × 2.1 μm^3. All imaging and analysis was performed blinded to the genotype of each sample.

4.7 | Image analysis: Optic fissure opening angle

3D data sets of live embryos labeled for cell membranes (EGFP-CAAX) were oriented in FluoRender[67] to achieve a lateral view. The lateral cutaway tool was used to cut to the lens midpoint. This orientation was captured in FluoRender and saved as a TIFF image. The optic fissure

opening angle was measured in Fiji using the angle tool; the vertex was positioned at the center of the lens with the rays of the angle projected to each optic fissure margin.

4.8 | Image analysis: Optic stalk volume

In Fiji, the segmentation editor was used to segment the optic stalk in 3D data sets of live embryos labeled for cell membranes (EGFP-CAAX). The optic stalk was outlined using the polygon selection function moving through the z-stack, slice by slice. Once the entire optic stalk was segmented, the stack was saved as a new tiff file. The total volume of the segmented region was measured in FluoRender using the volume size tool.

4.9 | Image analysis: Laminin fluorescence intensity

Laminin fluorescence intensity was measured in Fiji. Embryos were embedded and imaged laterally, so 3D rendering was not used for this analysis. First, optic fissure margin apposition was assayed blindly; we found that *pax2a*^{tu29a}, *pax2b*^{sa10953}, and *pax2a*^{tu29a}*; pax2b*^{sa10953} mutant embryos do not exhibit any defect in optic fissure margin apposition at the timepoints analyzed; therefore, we could use locations of margin apposition as landmarks. We then calculated a total range of the optic fissure depth within the optic cup, in which the most distal landmark was the depth at which the margins are in apposition and the retina is of maximum thickness, while the most proximal landmark was a section in which the optic fissure is no longer visible but the optic nerve head is present. The median was chosen as the middle z-slice. The total optic fissure depth within the optic cup was consistent for samples despite differences in genotype. In each slice that was quantified, the image was rotated such that the optic fissure aligned vertically through a rectangular ROI (area = 300 μm^2, schematized in Figure 2M) that was held constant for each image, across all samples. The ROI was placed to encompass the dorsal-ventral length of the optic fissure. Fluorescence intensity was calculated using the measure function in Fiji, taking the integrated mean density of the Laminin and TO-PRO-3 channel. Normalization was performed as a ratio of Laminin integrated mean density to TO-PRO-3 integrated mean density.

4.10 | Image analysis: *Tg(sox10:GFP)*-positive cell quantification

3D data sets were laterally oriented in FluoRender, and *Tg(sox10:GFP)*-positive cells were quantified by manually counting cells present throughout the depth of the optic fissure within the optic cup. Individual cells were identified by stepping through the z-plane through the lateral depth of the optic fissure using the clipping plane function in FluoRender, using both the cytoplasmic *sox10* transgenic label and mCherry-CAAX membrane marker to distinguish and resolve individual cells. Quantifications were performed blind to genotype, therefore any potential ambiguities resulting in under- or over-counting were equivalent across genotypes.

4.11 | Image analysis: *Tg(kdrl:mCherry-ras)* fluorescence intensity

Fluorescence intensity of *Tg(kdrl:mCherry-ras)* signal was measured in Fiji using a maximum intensity projection through the depth of the optic fissure within the optic cup. Embryos were embedded and imaged laterally, so 3D rendering was not used for this analysis. The range of slices used in the projection was determined such that the most distal slice represented the depth where the fissure margins are in apposition and the retina is of maximum thickness, and the most proximal slice is where the margins are no longer visible at the depth of the optic nerve head. The projection was rotated such that the optic fissure aligned vertically through a rectangular ROI (schematized in Figure 4M-O, area = 4400 μm^2 for 24 and 36 hpf, area = 1500 μm^2 for 48 hpf) that was held constant for each image. For 24 and 36 hpf images, the ROI encompassed the optic fissure and the ventral hemisphere of the lens; for 48 hpf images, the ROI encompassed the fissure only to eliminate abundant fluorescence of the hyaloid basket behind the lens at this stage. Fluorescence intensity was calculated using the measure function in Fiji, taking the integrated mean density of the mCherry and EGFP-CAAX channels. Normalization was performed as a ratio of mCherry integrated mean density to EGFP-CAAX integrated mean density. The EGFP-CAAX signal is produced from a stable transgene, thus variability in fluorescence is sufficiently controlled.

4.12 | Image analysis: Activated Caspase-3-positive cell quantification

Activated Caspase-3-positive cells were quantified in Fiji by manually counting labeled cells present throughout the depth of the optic fissure within the optic cup. Activated Caspase-3-positive cells in the forebrain, MHB, and POM were quantified by categorically classifying embryos as having >5 or <5 positive cells in each region, with the rationale that <5 positive cells represented a background

level of apoptosis occurring normally. Localization of activated Caspase-3-positive cells within the brain, eye, or optic stalk was determined via the nuclear channel and the organization of neuroepithelial tissue nuclei. POM cells were identified based on their localization surrounding and adjacent to, but not part of, the brain, eye, and optic stalk.

4.13 | Box and whisker plots

Box and whisker plots were generated using the ggplot2 package in R Studio. The lower and upper hinges correspond to the first and third quartiles. The upper whisker extends from the hinge to the largest value no further than 1.5 × IQR from the hinge, and the lower whisker extends from the hinge to the smallest value at most 1.5 × IQR of the hinge. Data beyond the end of the whiskers are called "outlying" points and are plotted individually. The line in the box represents the median.

4.14 | Statistics

For all quantifications, *P*-values were calculated using an unpaired student's *t*-test in which the means of the two comparisons are considered statistically significant if $P < .05$. If the variance of the two comparisons were significantly different, Welch's correction was used.

ACKNOWLEDGMENTS

The authors are grateful to Bruce Riley, Rod Stewart, Angie Serrano and Joe Yost for generously sharing reagents; Ben Jussila for early conceptualization of this project; and members of the Kwan lab for their useful discussions. The authors also thank the Centralized Zebrafish Animal Resource, and the DNA Sequencing Core at the University of Utah. This work was supported by a University of Utah Developmental Biology Training Grant (National Institutes of Health, T32 HD007491 to S.L.) and the National Eye Institute/National Institutes of Health (F31 EY030758 to S.L., R01 EY025378 to K.M.K.).

AUTHOR CONTRIBUTIONS

Sarah Lusk: Conceptualization (lead); data curation (lead); formal analysis (lead); funding acquisition (equal); investigation (lead); methodology (lead); project administration (supporting); supervision (lead); validation (lead); visualization (equal); writing – original draft (lead); writing – review and editing (equal). **Kristen Kwan:** Conceptualization (lead); data curation (supporting); formal analysis (supporting); funding acquisition (equal); investigation (supporting); methodology (equal); project administration (lead); resources (lead); supervision (equal); validation (supporting); visualization (equal); writing – original draft (supporting); writing – review and editing (equal).

ORCID

Sarah Lusk https://orcid.org/0000-0002-0602-4391
Kristen M. Kwan https://orcid.org/0000-0003-0052-275X

REFERENCES

1. Adler R, Canto-Soler MV. Molecular mechanisms of optic vesicle development: complexities, ambiguities and controversies. *Dev Biol*. 2007;305(1):1-13. https://doi.org/10.1016/j.ydbio.2007.01.045
2. Bazin-Lopez N, Valdivia LE, Wilson SW, Gestri G. Watching eyes take shape. *Curr Opin Genet Dev*. 2015;32:73-79. https://doi.org/10.1016/j.gde.2015.02.004
3. Casey MA, Lusk S, Kwan KM. Build me up optic cup: intrinsic and extrinsic mechanisms of vertebrate eye morphogenesis. *Dev Biol*. 2021;476:128-136. https://doi.org/10.1016/j.ydbio.2021.03.023
4. Chow RL, Lang RA. Early eye development in vertebrates. *Annu Rev Cell Dev Biol*. 2001;17:255-296. https://doi.org/10.1146/annurev.cellbio.17.1.255
5. Fuhrmann S. Eye morphogenesis and patterning of the optic vesicle. *Curr Top Dev Biol*. 2010;93:61-84. https://doi.org/10.1016/B978-0-12-385044-7.00003-5
6. Martinez-Morales JR, Wittbrodt J. Shaping the vertebrate eye. *Curr Opin Genet Dev*. 2009;19(5):511-517. https://doi.org/10.1016/j.gde.2009.08.003
7. Sinn R, Wittbrodt J. An eye on eye development. *Mech Dev*. 2013;130(6–8):347-358. https://doi.org/10.1016/j.mod.2013.05.001
8. Yang XJ. Roles of cell-extrinsic growth factors in vertebrate eye pattern formation and retinogenesis. *Semin Cell Dev Biol*. 2004;15(1):91-103. https://doi.org/10.1016/j.semcdb.2003.09.004
9. AS AS, Gregory-Evans CY, Gregory-Evans K. An update on the genetics of ocular coloboma. *Hum Genet*. 2019;138(8–9):865-880. https://doi.org/10.1007/s00439-019-02019-3
10. Chang L, Blain D, Bertuzzi S, Brooks BP. Uveal coloboma: clinical and basic science update. *Curr Opin Ophthalmol*. 2006;17(5):447-470. https://doi.org/10.1097/01.icu.0000243020.82380.f6
11. Fitzpatrick DR, van Heyningen V. Developmental eye disorders. *Curr Opin Genet Dev*. 2005;15(3):348-353. https://doi.org/10.1016/j.gde.2005.04.013
12. Gregory-Evans CY, Williams MJ, Halford S, Gregory-Evans K. Ocular coloboma: a reassessment in the age of molecular neuroscience. *J Med Genet*. 2004;41(12):881-891. https://doi.org/10.1136/jmg.2004.025494
13. Onwochei BC, Simon JW, Bateman JB, Couture KC, Mir E. Ocular colobomata. *Surv Ophthalmol*. 2000;45(3):175-194. https://doi.org/10.1016/s0039-6257(00)00151-x
14. Bernstein CS, Anderson MT, Gohel C, Slater K, Gross JM, Agarwala S. The cellular bases of choroid fissure formation and closure. *Dev Biol*. 2018;440(2):137-151. https://doi.org/10.1016/j.ydbio.2018.05.010

15. Hardy H, Prendergast JG, Patel A, et al. Detailed analysis of chick optic fissure closure reveals Netrin-1 as an essential mediator of epithelial fusion. *Elife*. 2019;8:e43877. https://doi.org/10.7554/eLife.43877
16. Geeraets R. An electron microscopic study of the closure of the optic fissure in the golden hamster. *Am J Anat*. 1976;145(4):411-431. https://doi.org/10.1002/aja.1001450402
17. Hero I. The optic fissure in the normal and microphthalmic mouse. *Exp Eye Res*. 1989;49(2):229-239. https://doi.org/10.1016/0014-4835(89)90093-6
18. Hero I. Optic fissure closure in the normal cinnamon mouse. An ultrastructural study. *Invest Ophthalmol Vis Sci*. 1990;31(1):197-216.
19. James A, Lee C, Williams AM, Angileri K, Lathrop KL, Gross JM. The hyaloid vasculature facilitates basement membrane breakdown during choroid fissure closure in the zebrafish eye. *Dev Biol*. 2016;419(2):262-272. https://doi.org/10.1016/j.ydbio.2016.09.008
20. Gestri G, Bazin-Lopez N, Scholes C, Wilson SW. Cell behaviors during closure of the choroid fissure in the developing eye. *Front Cell Neurosci*. 2018;12:42. https://doi.org/10.3389/fncel.2018.00042
21. Evans AL, Gage PJ. Expression of the homeobox gene Pitx2 in neural crest is required for optic stalk and ocular anterior segment development. *Hum Mol Genet*. 2005;14(22):3347-3359. https://doi.org/10.1093/hmg/ddi365
22. Lupo G, Gestri G, O'Brien M, et al. Retinoic acid receptor signaling regulates choroid fissure closure through independent mechanisms in the ventral optic cup and periocular mesenchyme. *Proc Natl Acad Sci U S A*. 2011;108(21):8698-8703. https://doi.org/10.1073/pnas.1103802108
23. McMahon C, Gestri G, Wilson SW, Link BA. Lmx1b is essential for survival of periocular mesenchymal cells and influences Fgf-mediated retinal patterning in zebrafish. *Dev Biol*. 2009;332(2):287-298. https://doi.org/10.1016/j.ydbio.2009.05.577
24. See AW, Clagett-Dame M. The temporal requirement for vitamin a in the developing eye: mechanism of action in optic fissure closure and new roles for the vitamin in regulating cell proliferation and adhesion in the embryonic retina. *Dev Biol*. 2009;325(1):94-105. https://doi.org/10.1016/j.ydbio.2008.09.030
25. Hero I, Farjah M, Scholtz CL. The prenatal development of the optic fissure in colobomatous microphthalmia. *Invest Ophthalmol Vis Sci*. 1991;32(9):2622-2635.
26. Weaver ML, Piedade WP, Meshram NN, Famulski JK. Hyaloid vasculature and mmp2 activity play a role during optic fissure fusion in zebrafish. *Sci Rep*. 2020;10(1):10136. https://doi.org/10.1038/s41598-020-66451-6
27. Bryan CD, Casey MA, Pfeiffer RL, Jones BW, Kwan KM. Optic cup morphogenesis requires neural crest-mediated basement membrane assembly. *Development*. 2020;147(4):dev181420. https://doi.org/10.1242/dev.181420
28. Gage PJ, Rhoades W, Prucka SK, Hjalt T. Fate maps of neural crest and mesoderm in the mammalian eye. *Invest Ophthalmol Vis Sci*. 2005;46(11):4200-4208. https://doi.org/10.1167/iovs.05-0691
29. Johnston MC, Noden DM, Hazelton RD, Coulombre JL, Coulombre AJ. Origins of avian ocular and periocular tissues. *Exp Eye Res*. 1979;29(1):27-43. https://doi.org/10.1016/0014-4835(79)90164-7
30. Langenberg T, Kahana A, Wszalek JA, Halloran MC. The eye organizes neural crest cell migration. *Dev Dyn*. 2008;237(6):1645-1652. https://doi.org/10.1002/dvdy.21577
31. Dressler GR, Deutsch U, Chowdhury K, Nornes HO, Gruss P. Pax2, a new murine paired-box-containing gene and its expression in the developing excretory system. *Development*. 1990;109(4):787-795.
32. Heller N, Brandli AW. Xenopus Pax-2 displays multiple splice forms during embryogenesis and pronephric kidney development. *Mech Dev*. 1997;69(1–2):83-104. https://doi.org/10.1016/s0925-4773(97)00158-5
33. Herbrand H, Guthrie S, Hadrys T, et al. Two regulatory genes, cNkx5-1 and cPax2, show different responses to local signals during otic placode and vesicle formation in the chick embryo. *Development*. 1998;125(4):645-654.
34. Krauss S, Johansen T, Korzh V, Fjose A. Expression of the zebrafish paired box gene pax[zf-b] during early neurogenesis. *Development*. 1991;113(4):1193-1206.
35. Macdonald R, Barth KA, Xu Q, Holder N, Mikkola I, Wilson SW. Midline signalling is required for Pax gene regulation and patterning of the eyes. *Development*. 1995;121(10):3267-3278.
36. Macdonald R, Scholes J, Strahle U, et al. The Pax protein Noi is required for commissural axon pathway formation in the rostral forebrain. *Development*. 1997;124(12):2397-2408.
37. Majumdar A, Lun K, Brand M, Drummond IA. Zebrafish no isthmus reveals a role for pax2.1 in tubule differentiation and patterning events in the pronephric primordia. *Development*. 2000;127(10):2089-2098.
38. Nornes HO, Dressler GR, Knapik EW, Deutsch U, Gruss P. Spatially and temporally restricted expression of *Pax2* during murine neurogenesis. *Development*. 1990;109(4):797-809.
39. Puschel AW, Westerfield M, Dressler GR. Comparative analysis of Pax-2 protein distributions during neurulation in mice and zebrafish. *Mech Dev*. 1992;38(3):197-208. https://doi.org/10.1016/0925-4773(92)90053-m
40. Brand M, Heisenberg CP, Jiang YJ, et al. Mutations in zebrafish genes affecting the formation of the boundary between midbrain and hindbrain. *Development*. 1996;123:179-190.
41. Favor J, Sandulache R, Neuhauser-Klaus A, et al. The mouse Pax2(1Neu) mutation is identical to a human *PAX2* mutation in a family with renal-coloboma syndrome and results in developmental defects of the brain, ear, eye, and kidney. *Proc Natl Acad Sci U S A*. 1996;93(24):13870-13875. https://doi.org/10.1073/pnas.93.24.13870
42. Lun K, Brand M. A series of no isthmus (noi) alleles of the zebrafish pax2.1 gene reveals multiple signaling events in development of the midbrain-hindbrain boundary. *Development*. 1998;125(16):3049-3062.
43. Torres M, Gomez-Pardo E, Dressler GR, Gruss P. Pax-2 controls multiple steps of urogenital development. *Development*. 1995;121(12):4057-4065.
44. Torres M, Gomez-Pardo E, Gruss P. *Pax2* contributes to inner ear patterning and optic nerve trajectory. *Development*. 1996;122(11):3381-3391.
45. Benetti E, Artifoni L, Salviati L, et al. Renal hypoplasia without optic coloboma associated with *PAX2* gene deletion. *Nephrol Dial Transplant*. 2007;22(7):2076-2078. https://doi.org/10.1093/ndt/gfm187

46. Sanyanusin P, McNoe LA, Sullivan MJ, Weaver RG, Eccles MR. Mutation of *PAX2* in two siblings with renal-coloboma syndrome. *Hum Mol Genet*. 1995;4(11):2183-2184. https://doi.org/10.1093/hmg/4.11.2183
47. Sanyanusin P, Schimmenti LA, McNoe LA, et al. Mutation of the *PAX2* gene in a family with optic nerve colobomas, renal anomalies and vesicoureteral reflux. *Nat Genet*. 1995;9(4):358-364. https://doi.org/10.1038/ng0495-358
48. Schimmenti LA. Renal coloboma syndrome. *Eur J Hum Genet*. 2011;19(12):1207-1212. https://doi.org/10.1038/ejhg.2011.102
49. Keller SA, Jones JM, Boyle A, et al. Kidney and retinal defects (Krd), a transgene-induced mutation with a deletion of mouse chromosome 19 that includes the *Pax2* locus. *Genomics*. 1994;23(2):309-320. https://doi.org/10.1006/geno.1994.1506
50. Gregory-Evans CY, Moosajee M, Shan X, Gregory-Evans K. Gene-specific differential response to anti-apoptotic therapies in zebrafish models of ocular coloboma. *Mol Vis*. 2011;17:1473-1484.
51. Viringipurampeer IA, Ferreira T, DeMaria S, et al. *Pax2* regulates a fadd-dependent molecular switch that drives tissue fusion during eye development. *Hum Mol Genet*. 2012;21(10):2357-2369. https://doi.org/10.1093/hmg/dds056
52. Pfeffer PL, Gerster T, Lun K, Brand M, Busslinger M. Characterization of three novel members of the zebrafish Pax2/5/8 family: dependency of Pax5 and Pax8 expression on the Pax2.1 (noi) function. *Development*. 1998;125(16):3063-3074.
53. Busch-Nentwich E, Kettleborough, R., Dooley, C. M., et al. Sanger institute zebrafish mutation project mutant data submission. *ZFIN Direct Data Submission* (http://zfinorg). 2013.
54. Moosajee M, Gregory-Evans K, Ellis CD, Seabra MC, Gregory-Evans CY. Translational bypass of nonsense mutations in zebrafish rep1, pax2.1 and lamb1 highlights a viable therapeutic option for untreatable genetic eye disease. *Hum Mol Genet*. 2008;17(24):3987-4000. https://doi.org/10.1093/hmg/ddn302
55. Dutton JR, Antonellis A, Carney TJ, et al. An evolutionarily conserved intronic region controls the spatiotemporal expression of the transcription factor *Sox10*. *BMC Dev Biol*. 2008;8:105. https://doi.org/10.1186/1471-213X-8-105
56. Chi NC, Shaw RM, De Val S, et al. Foxn4 directly regulates tbx2b expression and atrioventricular canal formation. *Genes Dev*. 2008;22(6):734-739. https://doi.org/10.1101/gad.1629408
57. Gordon HB, Lusk S, Carney KR, Wirick EO, Murray BF, Kwan KM. Hedgehog signaling regulates cell motility and optic fissure and stalk formation during vertebrate eye morphogenesis. *Development*. 2018;145(22):dev165068. https://doi.org/10.1242/dev.165068
58. Bosze B, Suarez-Navarro J, Soofi A, Lauderdale JD, Dressler GR, Brown NL. Multiple roles for *Pax2* in the embryonic mouse eye. *Dev Biol*. 2021;472:18-29. https://doi.org/10.1016/j.ydbio.2020.12.020
59. Torban E, Eccles MR, Favor J, Goodyer PR. *PAX2* suppresses apoptosis in renal collecting duct cells. *Am J Pathol*. 2000;157(3):833-842. https://doi.org/10.1016/S0002-9440(10)64597-X
60. Sidi S, Sanda T, Kennedy RD, et al. Chk1 suppresses a caspase-2 apoptotic response to DNA damage that bypasses p53, Bcl-2, and caspase-3. *Cell*. 2008;133(5):864-877. https://doi.org/10.1016/j.cell.2008.03.037
61. Bassett EA, Williams T, Zacharias AL, Gage PJ, Fuhrmann S, West-Mays JA. AP-2alpha knockout mice exhibit optic cup patterning defects and failure of optic stalk morphogenesis. *Hum Mol Genet*. 2010;19(9):1791-1804. https://doi.org/10.1093/hmg/ddq060
62. Brown JD, Dutta S, Bharti K, et al. Expression profiling during ocular development identifies 2 Nlz genes with a critical role in optic fissure closure. *Proc Natl Acad Sci U S A*. 2009;106(5):1462-1467. https://doi.org/10.1073/pnas.0812017106
63. Bouchard M, Grote D, Craven SE, Sun Q, Steinlein P, Busslinger M. Identification of Pax2-regulated genes by expression profiling of the mid-hindbrain organizer region. *Development*. 2005;132(11):2633-2643. https://doi.org/10.1242/dev.01833
64. Kimmel CB, Ballard WW, Kimmel SR, Ullmann B, Schilling TF. Stages of embryonic development of the zebrafish. *Dev Dyn*. 1995;203(3):253-310. https://doi.org/10.1002/aja.1002030302
65. Konieczny A, Ausubel FM. A procedure for mapping Arabidopsis mutations using co-dominant ecotype-specific PCR-based markers. *Plant J*. 1993;4(2):403-410. https://doi.org/10.1046/j.1365-313x.1993.04020403.x
66. Neff MM, Neff JD, Chory J, Pepper AE. dCAPS, a simple technique for the genetic analysis of single nucleotide polymorphisms: experimental applications in *Arabidopsis thaliana* genetics. *Plant J*. 1998;14(3):387-392. https://doi.org/10.1046/j.1365-313x.1998.00124.x
67. Wan Y, Otsuna H, Chien CB, Hansen C. FluoRender: an application of 2D image space methods for 3D and 4D confocal microscopy data visualization in neurobiology research. *IEEE Pac Vis Symp*. 2012;201-208. https://doi.org/10.1109/pacificvis.2012.6183592

How to cite this article: Lusk S, Kwan KM. *Pax2a*, but not *pax2b*, influences cell survival and periocular mesenchyme localization to facilitate zebrafish optic fissure closure. *Developmental Dynamics*. 2022;251(4):625-644. doi: 10.1002/dvdy.422